

Large-deformation reduced order homogenization of polycrystalline materials

Damin Xia^a, Xiang Zhang^b, Caglar Oskay^{a,*}

^a*Department of Civil and Environmental Engineering, Vanderbilt University, Nashville, TN 37235, United States of America*

^b*Department of Mechanical Engineering, University of Wyoming, 1000 E University Ave, Laramie, WY 82071*

Abstract

In this manuscript, we present a finite strain formulation of a reduced order computational homogenization model for crystal plasticity. The proposed formulation leverages and generalizes the principles of the Eigenstrain-based reduced order homogenization (EHM) approach. Asymptotic analysis with multiple scales is employed to describe the microscale problem in the deformed configuration. A two-term Taylor series approximation of the constitutive behavior along with a geometry-based basis reduction is employed to arrive at the reduced order model. An efficient implementation scheme is proposed to evaluate the multiscale system without the need to recompute the reduced basis as a function of evolving deformation. The ability of the proposed modeling approach in capturing homogenized and localized behavior as well as texture evolution is demonstrated in the context of single crystal and polycrystal microstructures.

Keywords: Crystal plasticity, Large deformation, Computational homogenization, Reduced order modeling.

1. Introduction

Reliably predicting the mechanical behavior of structures made of polycrystalline materials presents many challenges and complications. These complications are exacerbated in problems that exhibit and are affected by global-local features, where phenomena at small (e.g., microscopic) and large (i.e., structural) scales interact. Example applications include but not limited to forming of highly anisotropic metals, fatigue failure initiation, and shear dominated failure in metals subjected to high rate impact. Multiscale computational methods such as computational homogenization [1], variational multiscale enrichment [2–5], multiscale finite elements [6], heterogeneous multiscale [7] and others directly bridge these disparate scales and offer rigorous ways to tackle these challenging problems. This manuscript is concerned with formulating an efficient

*Correspondence to: VU Station B#351831, 2301 Vanderbilt Place, Nashville, TN 37235, United States of America.

Email address: caglar.oskay@vanderbilt.edu (Caglar Oskay)

computational homogenization model for nonlinear, large deformation response of polycrystalline materials.

Crystal plasticity finite element (CPFE) method [8–11] has been the computational workhorse for modeling the complex and highly heterogeneous behavior of polycrystalline materials at fine scales (see e.g., [12–14] among many others). Because of highly complex microstructural morphologies and evolution laws that govern viscoplastic and failure processes, CPFE simulations are typically computationally expensive even to track the behavior within a single characteristic volume (i.e., a representative or statistical volume element). Direct incorporation of CPFE to the aforementioned multiscale methodologies therefore remains prohibitive for most engineering problems.

In order to alleviate the computational cost issue, several reduced order modeling (ROM) approaches have been proposed to efficiently approximate the mechanical response of polycrystalline materials at the fine scale. In the context of small deformation kinematics, early attempts include the classical Sachs [15] and Taylor models [16], which provide bounds based on uniform kinetic and kinematic assumptions over the characteristic volume. More recent approaches such as viscoplastic self-consistent (VPSC) models [17, 18], fast Fourier transform method (FFT) [19, 20], nonuniform transformation field analysis [21, 22], proper orthogonal decomposition [23], self-consistent clustering method [24–26] employ a range of kinematic and kinetic approximations and computing algorithms aimed at reducing online computational cost of microstructure simulation with minimal accuracy loss. Eigendeformation-based homogenization method (EHM) is an alternative ROM approach that has been recently adapted to evaluate polycrystalline response [27]. In this approach the microstructure morphological information is retained in a small set of constitutive tensors that are pre-computed for a given characteristic volume. These tensors are then used to solve for the microscale response fields by evaluating a much smaller algebraic system of equations that approximate the microscopic equilibrium. An important advantage of the EHM approach is that it can keep the geometry information, grain interactions and intra-grain stress and strain variations during upscaling. More recent developments of the EHM approach include a sparse formulation that extends the computational advantages of EHM when solving large characteristic volumes [28], generalization to anisotropic crystals and multiphase microstructures [29], and extension to thermomechanics for analysis of large structural members operating in extreme environments [30]. In addition to reduced order modeling, application of data driven modeling principals to devise surrogate models provide a new and promising paradigm for drastic reduction of computational cost of microstructure simulation in the context of a multiscale analysis (see e.g., [31–33]).

More recently, a number of the aforementioned ROM approaches have been extended to account for large deformation and texture evolution. In VPSC, this is achieved by updating the Eshelby tensors associated with ellipsoidal inclusions that idealize each grain, where the shape parameters and crystal orientation evolve with deformation [34–38]. The FFT approach was extended to large deformation analysis of polycrystalline microstructures by Eisenlohr et al. [39] by extending the formulation proposed by Lahellec et al. [40]. Several integration schemes to accelerate the computations were proposed in Refs [41–47]. Recent publications develop grain cluster method [48, 49], self-consistent clustering method [50] and data-driven modeling [51, 52] for large deformation analyses as well.

In this manuscript, we propose a new reduced order multiscale formulation for large deformation response of polycrystalline materials undergoing texture evolution. The proposed formulation leverages the principles of EHM to achieve the model order reduction. A two-scale asymptotic analysis is performed over the original governing equations to decompose them into a microscopic problem (defined over the characteristic volume) and a macroscopic problem (defined over the macroscopic domain). Model order reduction is applied on the microscopic problem by employing the idea of representing the inelastic deformation rate using influence functions and a coarse basis approximation of the microscale kinematics. The constituent behavior is taken to be rigid-viscoplastic. The incremental constitutive form is approximated using a two-term Taylor series expansion, which allows us to express the rate of deformation with a form similar to the one used to express the microscopic strain tensor in small-strain EHM. Texture evolution is also accounted for in the present formulation. Accuracy and efficiency characteristics of the reduced order model predictions are assessed by comparing with CPFE simulations of various single- and polycrystal configurations. Numerical results demonstrate the capabilities of the proposed approach in efficiently capturing the overall as well as local mechanical response of the microstructure.

The manuscript is organized as follows: Section 2 describes the problem settings, where the kinematics and original constitutive equations are introduced. In Section 3, mathematical homogenization method with two-scale asymptotic analysis is employed, resulting in a coupled system of micro- and macroscale problems. The mapping function between the undeformed and deformed configurations of the characteristic volume is introduced. Section 4 provides the reconstruction of the microscale problem and the corresponding reduced basis approximation. Section 5 presents the numerical implementation strategy for the multiscale problem. In Section 6, the accuracy and efficiency of the proposed model are verified for voided single crystal and polycrystal microstructures in direct comparison with CPFE simulations. Section 7 provides conclusions and future work.

2. Problem statement

Figure 1 schematically illustrates the multiscale mechanical deformation problem. Consider a heterogeneous polycrystalline body, where the initial (undeformed) configuration is denoted as $\Omega_0 \subset \mathbb{R}^{n_{sd}}$ ($n_{sd} = 2, 3$ is the space dimension). Under the applied loading, the heterogeneous body undergoes large deformation. At time t , the current deformed configuration of the body is denoted as Ω . The position vectors that parameterize the initial and current configurations are, \mathbf{X} and \mathbf{x} , respectively. The deformation of the body is expressed as

$$x_i = \psi_i^\xi(\mathbf{X}, t) \quad (2.1)$$

in which, ψ^ξ is the deformation map. Superscript ξ indicates that the deformation response spatially fluctuates due to the heterogeneity of the material microstructure. The body is constructed by tiling a characteristic volume, CV (e.g., representative volume element, RVE or statistical volume element, SVE) that represents the microstructural morphology. The heterogeneity in the CV is due to the polycrystalline structure with misaligned crystals with varying grain sizes, multiple phases and other microstructural features. The domain of the periodic CV in its initial and current

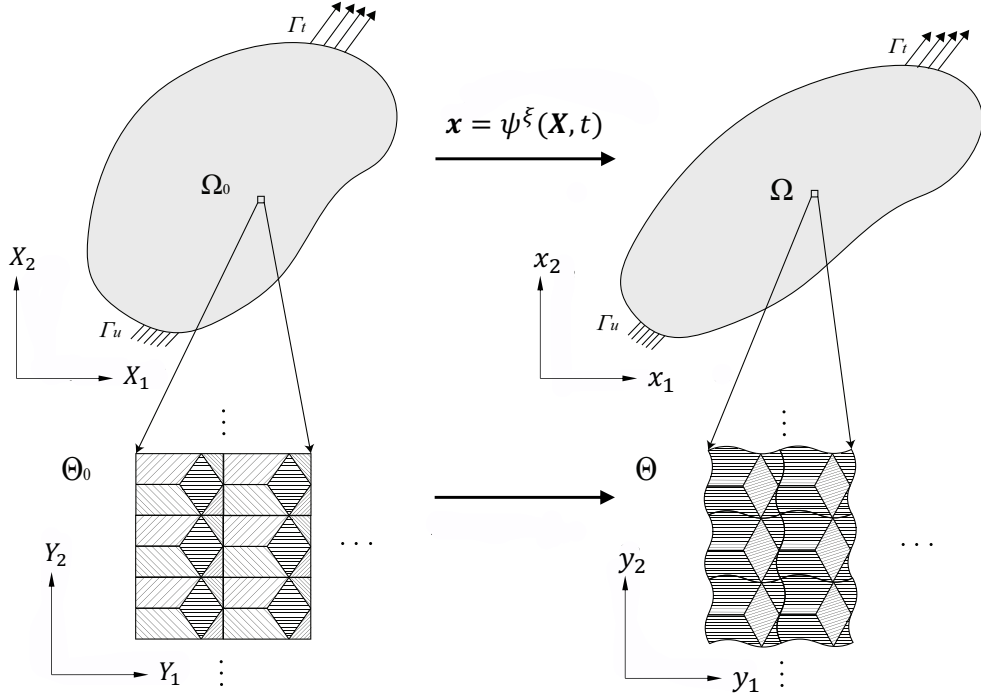


Figure 1: The two-scale problem: macro- and microscale problem domains in undeformed (left) and deformed (right) configurations.

states are respectively denoted as Θ_0 and Θ in scaled coordinates \mathbf{Y} and \mathbf{y} , respectively. The scaled, undeformed microscale coordinates are related to the original coordinates as

$$\mathbf{Y} := \frac{\mathbf{X}}{\xi} \quad \text{with} \quad 0 < \xi \ll 1 \quad (2.2)$$

in which ξ is the scaling parameter defined as the ratio between the size of the CV and the characteristic deformation wavelength. Let $f^\xi(\mathbf{X})$ denote an arbitrary response field defined in the undeformed configuration expressed in terms of a single scale coordinate. The function is expressed using the multiple spatial scales as

$$f^\xi(\mathbf{X}) = f\left(\mathbf{X}, \frac{\mathbf{X}}{\xi}\right) = f(\mathbf{X}, \mathbf{Y}) \quad (2.3)$$

Recalling Eq. (2.2) and using the chain rule, the gradient of the response field, $f^\xi(\mathbf{X})$ is

$$f_{,X_i}^\xi(\mathbf{X}) = f_{,X_i}(\mathbf{X}, \mathbf{Y}) + \frac{1}{\xi} f_{,Y_i}(\mathbf{X}, \mathbf{Y}) \quad (2.4)$$

All response fields are assumed to remain locally periodic throughout the deformation

$$f(\mathbf{X}, \mathbf{Y}) = f(\mathbf{X}, \mathbf{Y} + k\hat{\mathbf{Y}}) \quad \forall \mathbf{X} \in \Omega_0 \quad (2.5)$$

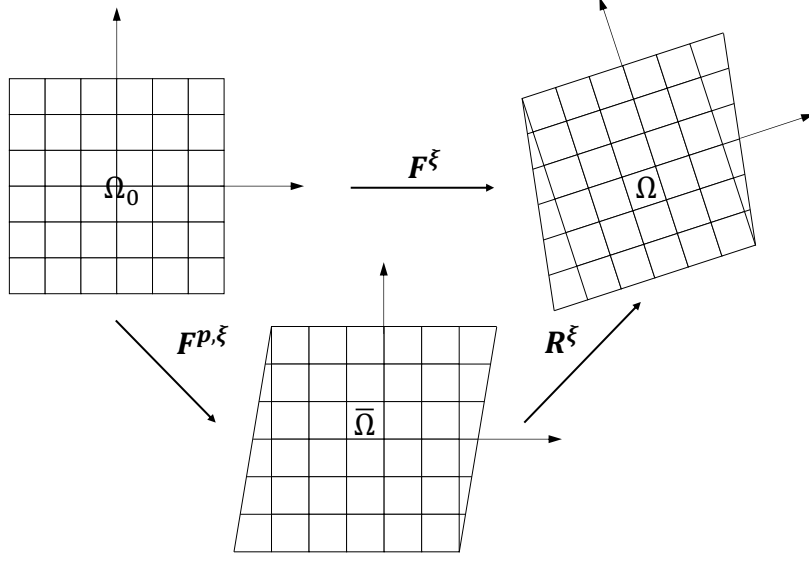


Figure 2: Kinematics of rigid-viscoplastic deformation of single crystal deformed by crystallographic slip.

where \hat{Y} is the period of the CV and \mathbf{k} is a $n_{sd} \times n_{sd}$ diagonal matrix with integer components.

In the current manuscript, we restrict the formulation such that the constituent materials within the CV are idealized as rigid-viscoplastic. The visco-plasticity within the crystals is represented by a crystal plasticity model. The elastic response of the domain is ignored as we are primarily concerned with the viscoplastic flow regime of the material behavior under large deformations [11]. Texture evolution is important when polycrystalline material undergoes large deformation, and is therefore considered and explicitly tracked.

2.1. Kinematics

Following Kok [53], we consider the multiplicative decomposition of the deformation gradient ($\mathbf{F}^{\xi} = \partial \mathbf{x} / \partial \mathbf{X}$) into a rigid body rotation part \mathbf{R}^{ξ} and a viscoplastic part $\mathbf{F}^{p,\xi}$

$$F_{ij}^{\xi} = R_{im}^{\xi} F_{mj}^{p,\xi} \quad (2.6)$$

The decomposition illustrated in Fig. 2 separates lattice rotation from plastic spin, and the former results in texture evolution. Employing the multiplicative decomposition of \mathbf{F}^{ξ} , the velocity gradient $\mathbf{L}^{\xi} := \partial \mathbf{v}^{\xi} / \partial \mathbf{x}$ (where, \mathbf{v}^{ξ} is velocity) is written as

$$L_{ij}^{\xi} = \dot{F}_{im}^{\xi} (F_{mj}^{\xi})^{-1} = \dot{R}_{im}^{\xi} R_{jm}^{\xi} + L_{ij}^{p,\xi} \quad (2.7)$$

where $\mathbf{L}^{p,\xi}$ is the viscoplastic velocity gradient

$$L_{ij}^{p,\xi} = R_{im}^{\xi} \dot{F}_{mk}^{p,\xi} (F_{kl}^{p,\xi})^{-1} R_{jl}^{\xi} \quad (2.8)$$

The rate of deformation tensor \mathbf{D}^ξ and the spin tensor \mathbf{W}^ξ are obtained from the velocity gradient as

$$D_{ij}^\xi = D_{ij}^{p,\xi} = \text{sym}(L_{ij}^{p,\xi}) = \text{sym}(L_{ij}^\xi); \quad W_{ij}^\xi = \Omega_{ij}^\xi + W_{ij}^{p,\xi} \quad (2.9)$$

and

$$W_{ij}^{p,\xi} = \text{skew}(L_{ij}^{p,\xi}) \quad (2.10)$$

$$\Omega_{ij}^\xi = \dot{R}_{im}^\xi R_{jm}^\xi \quad (2.11)$$

using $\text{sym}(\dot{\mathbf{R}}^\xi \mathbf{R}^\xi) = \mathbf{0}$. $\mathbf{D}^{p,\xi}$ is the rate of viscoplastic deformation tensor and $\mathbf{W}^{p,\xi}$ is the viscoplastic spin. Note that due to the equivalence between $\mathbf{D}^{p,\xi}$ and \mathbf{D}^ξ , we use \mathbf{D}^ξ to denote the viscoplastic deformation rate in the remainder of this manuscript.

2.2. Constitutive equations

While the current formulation can account for different sources of plastic deformation, we consider that the plastic deformation of a grain is only induced by the crystallographic slip along the lattice-dependent slip planes. The viscoplastic velocity gradient $\mathbf{L}^{p,\xi}$ is written as

$$L_{ij}^{p,\xi} = \sum_{s=1}^N Z_{ij}^{s,\xi}(\mathbf{x}, t) \dot{\gamma}^{s,\xi}(\mathbf{x}, t) \quad (2.12)$$

where N is the number of slip systems, $\dot{\gamma}^{s,\xi}$ is the slip rate of the s^{th} slip system, and $\mathbf{Z}^{s,\xi}$ is the Schmid tensor defined as the dyadic product of the slip direction $\mathbf{n}^{s,\xi}$ and normal to the slip plane $\mathbf{m}^{s,\xi}$ (i.e., $\mathbf{Z}^{s,\xi} = \mathbf{n}^{s,\xi} \otimes \mathbf{m}^{s,\xi}$) and represents the slip system orientation. Substituting Eq. (2.12) into Eq. (2.9) and (2.10) yields

$$D_{ij}^\xi = \sum_{s=1}^N \text{sym}(Z_{ij}^{s,\xi}(\mathbf{x}, t)) \dot{\gamma}^{s,\xi}(\mathbf{x}, t) \quad (2.13)$$

$$W_{ij}^{p,\xi} = \sum_{s=1}^N \text{skew}(Z_{ij}^{s,\xi}(\mathbf{x}, t)) \dot{\gamma}^{s,\xi}(\mathbf{x}, t) \quad (2.14)$$

The slip rate $\dot{\gamma}^{s,\xi}$ is described by a flow rule as a function of resolved shear stress $\tau^{s,\xi}$ and the slip system strength $g^{s,\xi}$. While the present formulation allows arbitrary forms for flow and hardening evolution, we adopt a frequently used flow rule suggested by Rice and Peirce [8, 54] for simplicity

$$\dot{\gamma}^{s,\xi} = \dot{\gamma}_0 \left(\frac{|\tau^{s,\xi}(\mathbf{x}, t)|}{g^{s,\xi}} \right)^{\frac{1}{m}} \text{sgn}(\tau^{s,\xi}(\mathbf{x}, t)) \quad (2.15)$$

in which, m is the rate sensitivity parameter, and $\dot{\gamma}_0$ is the reference slip rate. The resolved shear stress is the projection of the Cauchy stress $\boldsymbol{\sigma}^\xi$ onto an individual slip system through the Schmid tensor

$$\tau^{s,\xi}(\mathbf{x}, t) = \boldsymbol{\sigma}_{ij}^\xi(\mathbf{x}, t) Z_{ij}^{s,\xi}(\mathbf{x}, t) \quad (2.16)$$

The evolution of the slip system strength follows a hardening rule considering latent hardening

proposed by Anand [55]

$$\dot{g}^{s,\xi} = h_0 \left(\frac{g_{sa}^{s,\xi} - g^{s,\xi}}{g_{sa}^{s,\xi} - g_0^{s,\xi}} \right) \sum_{s=1}^N |\dot{\gamma}^{s,\xi}| \quad (2.17)$$

where h_0 is the initial hardening rate, $g_{sa}^{s,\xi}$ is the saturation stress of the s^{th} slip system, and $g_0^{s,\xi}$ is the initial strength of s^{th} slip system. The saturation stress is further defined as

$$g_{sa}^{s,\xi} = g_{sa,0}^s \left(\sum_{s=1}^N \frac{|\dot{\gamma}^{s,\xi}|}{\dot{\gamma}_{s0}} \right)^{m'} \quad (2.18)$$

in which $g_{sa,0}^s$, $\dot{\gamma}_{s0}$ and m' are material parameters.

The evolution of the texture is described by the evolution of the Schmid tensor $\mathbf{Z}^{s,\xi}$. Let the crystal orientation be described by Euler angles (ψ_1, ϕ, ψ_2) , from which the rotation tensor \mathbf{C}^ξ is constructed (detailed expression is stated in Section 5). The rotation matrix is used to transform the orthonormal slip system vectors $(\mathbf{n}_0^{s,\xi}, \mathbf{m}_0^{s,\xi})$ from lattice axis to sample axis

$$n_i^{s,\xi} = C_{ij}^\xi n_{0j}^{s,\xi}; \quad m_i^{s,\xi} = C_{ij}^\xi m_{0j}^{s,\xi} \quad (2.19)$$

Hence, the Schmid tensor is rotated as

$$Z_{ij}^{s,\xi} = C_{im}^\xi Z_{0mn}^{s,\xi} C_{jn}^\xi \quad (2.20)$$

where $\mathbf{Z}_0^{s,\xi} = \mathbf{n}_0^{s,\xi} \otimes \mathbf{m}_0^{s,\xi}$ describes the slip system orientation with respect to the lattice axis. Equation (2.20) indicates that the Schmid tensor evolves with the rotation matrix \mathbf{C}^ξ , which is constructed by the rotation tensor \mathbf{R}^ξ as

$$C_{ij}^\xi = R_{im}^\xi C_{0mj}^\xi \quad (2.21)$$

where \mathbf{C}_0^ξ is the initial orientation and is prescribed as part of the crystal initial state.

2.3. Governing equilibrium and boundary conditions

The equilibrium is written in the deformed configuration using Cauchy stress as the stress measure

$$\sigma_{ij,x_j}^\xi(\mathbf{x}, t) + b_i^\xi(\mathbf{x}, t) = 0 \quad (2.22)$$

in which \mathbf{b}^ξ stands for the body force per unit volume. The boundary conditions for the boundary value problem are

$$\begin{aligned} u_i^\xi(\mathbf{x}, t) &= \bar{u}_i(\mathbf{x}, t) & \mathbf{x} \in \Gamma^u \\ \sigma_{ij}^\xi(\mathbf{x}, t) n_j &= \bar{t}_i(\mathbf{x}, t) & \mathbf{x} \in \Gamma^t \end{aligned} \quad (2.23)$$

in which $\bar{\mathbf{u}}$ and $\bar{\mathbf{t}}$ are the prescribed displacement and traction on the boundaries Γ^u and Γ^t , where $\Gamma^u \cup \Gamma^t = \partial\Omega$ and $\Gamma^u \cap \Gamma^t = \emptyset$. \mathbf{n} is the unit normal to Γ^t .

3. Mathematical homogenization with two scales

In this section, we employ the method of asymptotic analysis with multiple scales to analyze the system of equations defined in Section 2. Asymptotic analyses of large deformation problems have been previously performed (see e.g. [56, 57]), while in the previous studies, the analyses have been typically performed in the undeformed configuration. We perform the analysis in the deformed configuration in the current work. While equivalent, the resulting system at the microscale is more amenable to model order reduction using EHM. In what follows, we establish mapping functions between the deformed and undeformed configurations at two scales. Then the two scale asymptotic analysis is performed to decompose the governing equations defined in Section 2 to formulate the micro- and macroscale problems.

3.1. Mapping between undeformed configuration and deformed configuration

We start from a two-scale asymptotic expansion of the displacement field in the undeformed configuration

$$u_i^\xi(\mathbf{X}, t) = u_i(\mathbf{X}, \mathbf{Y}, t) = u_i^0(\mathbf{X}, t) + \xi u_i^1(\mathbf{X}, \mathbf{Y}, t) + O(\xi^2) \quad (3.1)$$

where \mathbf{u}^0 is the leading order displacement, which is taken to be independent of the microscale. The transformation from undeformed to deformed configuration is established by analyzing the deformation mapping. In the context of a two-scale asymptotic analysis, separate mapping between macro- (\mathbf{X} to \mathbf{x}) and microscopic (\mathbf{Y} to \mathbf{y}) coordinates are derived and employed. In the following derivations, we assume that the size of the characteristic volume is infinitesimal (i.e., $0 < \xi \ll 1$) compared to the deformation wavelength, and the leading order displacement field $\mathbf{u}^0(\mathbf{X}, t)$ is constant over the characteristic volume domain

$$u_i^0(\mathbf{X}_1, t) = u_i^0(\mathbf{X}_2, t) \quad \text{if} \quad \|\mathbf{X}_1 - \mathbf{X}_2\| < \xi \quad (3.2)$$

where, \mathbf{X}_1 and $\mathbf{X}_2 \in \Omega$ are two macroscopic material points close to each other. Consider the mapping $\boldsymbol{\psi}^\xi(\mathbf{X}, t)$ that transforms the undeformed configuration to the deformed configuration $\boldsymbol{\psi}^\xi(\mathbf{X}, t) = \boldsymbol{\psi}(\mathbf{X}, \mathbf{Y}, t)$. Since the difference between the deformed and undeformed configurations is the displacement field, the mapping function can also be written as

$$\boldsymbol{\psi}_i^\xi(\mathbf{X}, t) = X_i + u_i^\xi(\mathbf{X}, t) \quad (3.3)$$

Substituting Eq. (3.1) into Eq. (3.3) and using Eq. (2.1), we have

$$x_i = X_i + u_i^0(\mathbf{X}, t) + \xi u_i^1(\mathbf{X}, \mathbf{Y}, t) + O(\xi^2) \quad (3.4)$$

At the limit $\xi \rightarrow 0$, the macroscopic mapping is obtained as

$$x_i = \boldsymbol{\psi}_i^M(\mathbf{X}, t) = X_i + u_i^0(\mathbf{X}, t) \quad (3.5)$$

The mapping for the microscale coordinates (\mathbf{Y} to \mathbf{y}) is obtained by considering an arbitrary but fixed point $\hat{\mathbf{X}}$ in the immediate neighborhood of \mathbf{X} . The deformed and undeformed configurations,

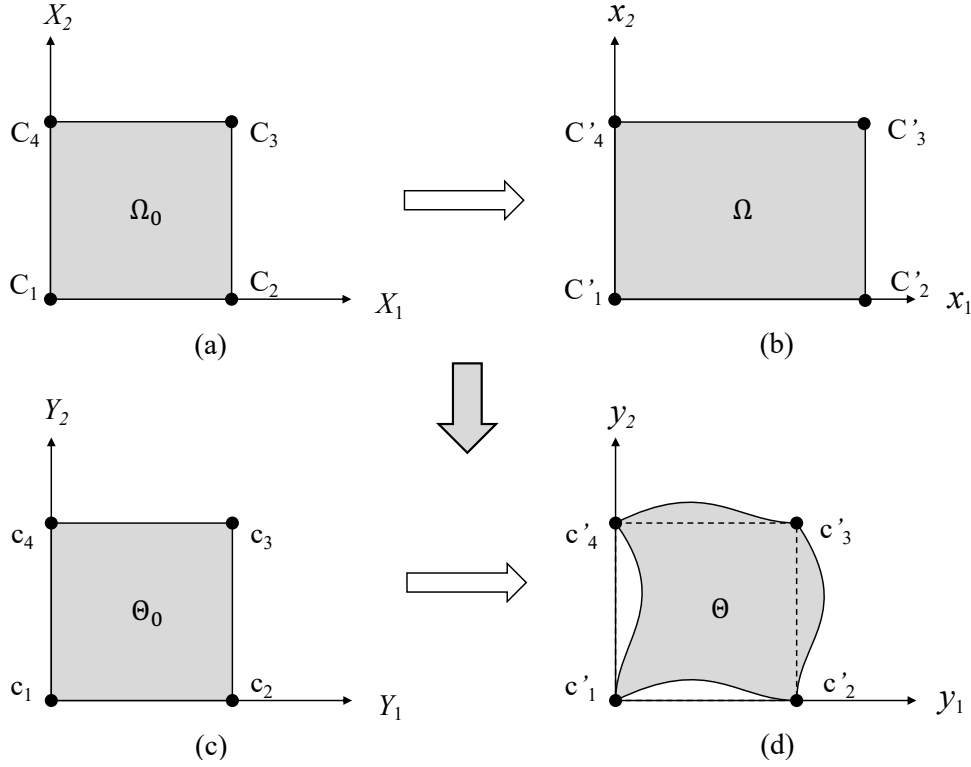


Figure 3: Mappings: (a) initial macrostructure; (b) deformed macrostructure; (c) initial microstructure and (d) deformed microstructure

$\hat{\mathbf{x}}$ and $\hat{\mathbf{X}}$, are connected by the macroscopic mapping function as

$$\hat{x}_i = \hat{X}_i + u_i^0(\hat{\mathbf{X}}, t) \quad (3.6)$$

Subtracting Eq. (3.6) from Eq. (3.4), we have

$$x_i - \hat{x}_i = X_i - \hat{X}_i + u_i^0(\mathbf{X}, t) - u_i^0(\hat{\mathbf{X}}, t) + \xi u_i^1(\mathbf{X}, \mathbf{Y}, t) + O(\xi^2) \quad (3.7)$$

Considering Eq. (3.2) and the identities $\mathbf{x} - \hat{\mathbf{x}} = \xi \mathbf{y}$ and $\mathbf{X} - \hat{\mathbf{X}} = \xi \mathbf{Y}$, and using asymptotic matching of $O(\xi)$ terms yield

$$y_i = \psi_i^m(\mathbf{X}, \mathbf{Y}, t) = Y_i + u_i^1(\mathbf{X}, \mathbf{Y}, t) \quad (3.8)$$

which is the microscopic mapping. Equation (3.8) shows that the microscale deformation is described by the fluctuating microscopic perturbation of the displacement field, \mathbf{u}^1 . Figure 3 is a schematic illustration of the mapping, where the macrostructure undergoes some deformation due to \mathbf{u}^0 (e.g. uniaxial tension), and microstructure undergoes microscopic periodic deformation due to \mathbf{u}^1 .

3.2. Two-scale asymptotic analysis in the deformed configuration

Taking the time derivative of Eq. (3.1) yields the asymptotic expansion of the velocity field

$$\hat{v}_i^\xi(\mathbf{X}, t) = \hat{v}_i(\mathbf{X}, \mathbf{Y}, t) = \hat{v}_i^0(\mathbf{X}, t) + \xi \hat{v}_i^1(\mathbf{X}, \mathbf{Y}, t) + O(\xi^2) \quad (3.9)$$

where $\hat{\mathbf{v}} = \dot{\mathbf{u}}$ is the velocity field defined in the undeformed configuration. Utilizing the micro- and macro- mapping functions in Eq. (3.5) and Eq. (3.8), the asymptotic expansion of the velocity field in the deformed configuration is written as

$$v_i^\xi(\mathbf{x}, t) = v_i(\mathbf{x}, \mathbf{y}, t) = v_i^0(\mathbf{x}, t) + \xi v_i^1(\mathbf{x}, \mathbf{y}, t) + O(\xi^2) \quad (3.10)$$

It is important to note that the scale separated mappings allow a consistent and one-to-one correspondence of the asymptotic terms of the velocity field between the undeformed and deformed configurations

$$\hat{v}_i^0\left(\left(\psi^M\right)^{-1}(\mathbf{x}), t\right) = v_i^0(\mathbf{x}, t) \quad (3.11)$$

$$\hat{v}_i^1\left(\left(\psi^M\right)^{-1}(\mathbf{x}), \left(\psi^m\right)^{-1}(\mathbf{y}), t\right) = v_i^1(\mathbf{x}, \mathbf{y}, t) \quad (3.12)$$

Considering the rate of deformation tensor and the spin tensor are the symmetrical and skew parts of the velocity gradient, respectively, we can write

$$D_{ij}^\xi = v_{\langle i,j \rangle}^\xi(\mathbf{x}, t) := \frac{1}{2} \left(v_{i,j}^\xi(\mathbf{x}, t) + v_{j,i}^\xi(\mathbf{x}, t) \right) \quad (3.13)$$

$$W_{ij}^\xi = v_{\langle i,j \rangle}^\xi(\mathbf{x}, t) := \frac{1}{2} \left(v_{i,j}^\xi(\mathbf{x}, t) - v_{j,i}^\xi(\mathbf{x}, t) \right) \quad (3.14)$$

Substituting Eq. (3.10) into Eqs. (3.13) and (3.14) yields

$$D_{ij}^\xi(\mathbf{x}, t) = D_{ij}(\mathbf{x}, \mathbf{y}, t) = D_{ij}^0(\mathbf{x}, \mathbf{y}, t) + \xi D_{ij}^1(\mathbf{x}, \mathbf{y}, t) + O(\xi^2) \quad (3.15)$$

$$W_{ij}^\xi(\mathbf{x}, t) = W_{ij}(\mathbf{x}, \mathbf{y}, t) = W_{ij}^0(\mathbf{x}, \mathbf{y}, t) + \xi W_{ij}^1(\mathbf{x}, \mathbf{y}, t) + O(\xi^2) \quad (3.16)$$

where

$$D_{ij}^k(\mathbf{x}, \mathbf{y}, t) = v_{\langle i,x_j \rangle}^k + v_{\langle i,y_j \rangle}^{k+1}; \quad k = 0, 1 \quad (3.17)$$

$$W_{ij}^k(\mathbf{x}, \mathbf{y}, t) = v_{\langle i,x_j \rangle}^k - v_{\langle i,y_j \rangle}^{k+1}; \quad k = 0, 1 \quad (3.18)$$

Considering the periodicity over the deformed microstructure, the macroscopic rate of deformation tensor and the spin tensor are defined as

$$\begin{aligned} \bar{D}_{ij}(\mathbf{x}, t) &:= \lim_{\xi \rightarrow 0} \left\langle D_{ij}(\mathbf{x}, \mathbf{y}, t) \right\rangle_{\Theta} = v_{\langle i,x_j \rangle}^0(\mathbf{x}, t); \\ \bar{W}_{ij}(\mathbf{x}, t) &:= \lim_{\xi \rightarrow 0} \left\langle W_{ij}(\mathbf{x}, \mathbf{y}, t) \right\rangle_{\Theta} = v_{\langle i,x_j \rangle}^0(\mathbf{x}, t) \end{aligned} \quad (3.19)$$

in which $\langle \cdot \rangle_{\Theta}$ denotes spatial averaging over the deformed characteristic volume. In subsequent derivations, we place an overbar on a field quantity to indicate spatial averaging. Consider the asymptotic expansions for the Cauchy stress, slip system strength and the Schmid tensor

$$\sigma_{ij}^{\xi}(\mathbf{x}, t) = \sigma_{ij}(\mathbf{x}, \mathbf{y}, t) = \sigma_{ij}^0(\mathbf{x}, \mathbf{y}, t) + \xi \sigma_{ij}^1(\mathbf{x}, \mathbf{y}, t) + O(\xi^2) \quad (3.20)$$

$$g^{s,\xi}(\mathbf{x}, t) = g^s(\mathbf{x}, \mathbf{y}, t) = g^{s,0}(\mathbf{x}, \mathbf{y}, t) + \xi g^{s,1}(\mathbf{x}, \mathbf{y}, t) + O(\xi^2) \quad (3.21)$$

$$Z_{ij}^{s,\xi}(\mathbf{x}, t) = Z_{ij}^s(\mathbf{x}, \mathbf{y}, t) = Z_{ij}^{s,0}(\mathbf{x}, \mathbf{y}, t) + \xi Z_{ij}^{s,1}(\mathbf{x}, \mathbf{y}, t) + O(\xi^2) \quad (3.22)$$

Substituting the asymptotic expansions into Eqs. (2.13) and (2.14), and considering the first order terms yield

$$D_{ij}^0(\mathbf{x}, \mathbf{y}, t) = \sum_{s=1}^N \text{sym} \left(Z_{ij}^{s,0}(\mathbf{x}, \mathbf{y}, t) \right) \dot{\gamma}^{s,0}(\mathbf{x}, \mathbf{y}, t) \quad (3.23)$$

$$W_{ij}^{p,0}(\mathbf{x}, \mathbf{y}, t) = \sum_{s=1}^N \text{skew} \left(Z_{ij}^{s,0}(\mathbf{x}, \mathbf{y}, t) \right) \dot{\gamma}^{s,0}(\mathbf{x}, \mathbf{y}, t) \quad (3.24)$$

in which, $\dot{\gamma}^{s,0}$ is the first order term of a Taylor Series approximation of the slip rate [27]

$$\dot{\gamma}^{s,0}(\mathbf{x}, \mathbf{y}, t) = \dot{\gamma}_0 \left(\frac{|\tau^{s,0}(\mathbf{x}, \mathbf{y}, t)|}{g^{s,0}} \right)^{\frac{1}{m}} \text{sgn}(\tau^{s,0}(\mathbf{x}, \mathbf{y}, t)) \quad (3.25)$$

where, $\tau^{s,0}$ is the leading order term of the resolved shear stress obtained by substituting Eqs. (3.20) and (3.22) into Eq. (2.16)

$$\tau^{s,0}(\mathbf{x}, \mathbf{y}, t) = \sigma_{ij}^0(\mathbf{x}, \mathbf{y}, t) Z_{ij}^{s,0}(\mathbf{x}, \mathbf{y}, t) \quad (3.26)$$

Considering a Taylor Series expansion of Eq. (2.17) around $g^{s,0}$, the first order term in the expansion provides the evolution equation for the leading order slip system strength term [27]

$$\dot{g}^{s,0} = h_0 \left(\frac{g_{sa}^{s,0} - g^{s,0}}{g_{sa}^{s,0} - g_0^{s,0}} \right) \sum_{s=1}^N |\dot{\gamma}^{s,0}| \quad (3.27)$$

in which the first order approximation of the saturation stress is

$$g_{sa}^{s,0} = g_{sa,0}^s \left(\sum_{s=1}^N \frac{|\dot{\gamma}^{s,0}|}{\dot{\gamma}_{s0}^{s,0}} \right)^m \quad (3.28)$$

We proceed with deriving the governing equations for texture update. Consider the asymptotic expansion for the rotation tensor \mathbf{R}^{ξ}

$$R_{ij}^{\xi}(\mathbf{x}, t) = R_{ij}^0(\mathbf{x}, \mathbf{y}, t) + \xi R_{ij}^1(\mathbf{x}, \mathbf{y}, t) + O(\xi^2) \quad (3.29)$$

and the first order approximations for \mathbf{W}^ξ and $\mathbf{W}^{p,\xi}$, employing Eqs. (2.9) and (2.11) we get

$$\dot{R}_{ij}^0 = (W_{im}^0 - W_{im}^{p,0})R_{mj}^0 \quad (3.30)$$

Substituting the asymptotic expansion of the stress field (Eq. (3.20)) into the equilibrium equation (Eq. (2.22)), employing the chain rule (Eq. (2.4)), and identifying equations with equal order of ξ yield

$$O(\xi^{-1}) : \sigma_{ij,y_j}^0(\mathbf{x}, \mathbf{y}, t) = 0 \quad (3.31)$$

$$O(1) : \sigma_{ij,x_j}^0(\mathbf{x}, \mathbf{y}, t) + \sigma_{ij,y_j}^1(\mathbf{x}, \mathbf{y}, t) + b_i(\mathbf{x}, \mathbf{y}, t) = 0 \quad (3.32)$$

The $O(\xi^{-1})$ equilibrium equation ensures microscopic equilibrium, whereas the homogenized macroscopic equilibrium is obtained by averaging $O(1)$ equation over the CV domain Θ and exploiting periodicity

$$\bar{\sigma}_{ij,x_j}(\mathbf{x}, t) + \bar{b}_i(\mathbf{x}, t) = 0 \quad (3.33)$$

The governing equations that result from the asymptotic analysis are collected to form the macroscopic (i.e., homogenized) problem summarized in Box I and the microscopic problem in Box II. The general procedure described above is similar to the first-order nonlinear homogenization discussed in [58], but expressed in the current frame and specialized for crystal plasticity. The microscale problem constitutes a well-defined boundary value problem posed over the CV, where the “forcing term is the homogenized rate of deformation, $\bar{\mathbf{D}}$. In the macroscopic problem, the macroscopic Cauchy stress, $\bar{\boldsymbol{\sigma}}$ is obtained by spatial averaging of the microscopic stress field provided by the microscale problem, tightly coupling the two scales.

Box I. Macroscale problem

Given: average body force, $\bar{\mathbf{b}}$, boundary conditions, $\bar{\mathbf{u}}, \bar{\mathbf{t}}$ at time $t \in [0, t_0]$;

Find: macroscopic displacement field $\mathbf{u}^0 : \Omega \times [0, t_0] \rightarrow \mathbb{R}^{n_{sd}}$ which satisfies

- Equilibrium ($\mathbf{x} \in \Omega; t \in [0, t_0]$)

$$\bar{\sigma}_{ij,x_j}(\mathbf{x}, t) + \bar{b}_i(\mathbf{x}, t) = 0;$$

- Kinematics ($\mathbf{x} \in \Omega; t \in [0, t_0]$)

$$\bar{D}_{ij} = \frac{1}{2} (v_{i,x_j}^0 + v_{j,x_i}^0); \quad \bar{W}_{ij} = \frac{1}{2} (v_{i,x_j}^0 - v_{j,x_i}^0);$$

- Constitutive relation ($\mathbf{x} \in \Omega; t \in [0, t_0]$)

$$\bar{\sigma}_{ij}(\mathbf{x}, t) = \frac{1}{|\Theta|} \int_{\Theta} \sigma_{ij}^0(\mathbf{x}, \mathbf{y}, t) d\mathbf{y};$$

- Boundary conditions

$$u_i^0(\mathbf{x}, t) = \bar{u}_i(\mathbf{x}, t) \quad \mathbf{x} \in \Gamma^u, t \in [0, t_0]; \quad \bar{\sigma}_{ij}(\mathbf{x}, t) n_j = \bar{t}_i(\mathbf{x}, t) \quad \mathbf{x} \in \Gamma^t, t \in [0, t_0];$$

Box II. Microscale problem

Given: material parameters $m, \dot{\gamma}_0, h_0, g_0^s, g_{sa,0}^s, m$ and $\dot{\gamma}_{s0}$, macroscopic strain rate $\bar{\mathbf{D}}(\mathbf{x}, t)$ at a fixed but arbitrary point, \mathbf{x}

Find: microscopic displacement field $\mathbf{u}^1 : \Theta \times [0, t_0] \rightarrow \mathbb{R}^{n_{sd}}$, which satisfies:

- Equilibrium

$$\sigma_{ij,y_j}^0(\mathbf{x}, \mathbf{y}, t) = 0;$$

- Kinematics

$$D_{ij}^0(\mathbf{x}, \mathbf{y}, t) = v_{(i,x_j)}^0(\mathbf{x}, t) + v_{(i,y_j)}^1(\mathbf{x}, \mathbf{y}, t);$$

$$W_{ij}^0(\mathbf{x}, \mathbf{y}, t) = v_{\langle i,x_j \rangle}^0(\mathbf{x}, t) + v_{\langle i,y_j \rangle}^1(\mathbf{x}, \mathbf{y}, t);$$

- Constitutive relations

$$D_{ij}^0(\mathbf{x}, \mathbf{y}, t) = \sum_{s=1}^N \text{sym} \left(Z_{ij}^{s,0}(\mathbf{x}, \mathbf{y}, t) \right) \dot{\gamma}^{s,0}(\mathbf{x}, \mathbf{y}, t);$$

$$W_{ij}^{p,0}(\mathbf{x}, \mathbf{y}, t) = \sum_{s=1}^N \text{skew} \left(Z_{ij}^{s,0}(\mathbf{x}, \mathbf{y}, t) \right) \dot{\gamma}^{s,0}(\mathbf{x}, \mathbf{y}, t);$$

$$\dot{R}_{ij}^0(\mathbf{x}, \mathbf{y}, t) = \left[W_{im}^0(\mathbf{x}, \mathbf{y}, t) - W_{im}^{p,0}(\mathbf{x}, \mathbf{y}, t) \right] R_{mj}^0(\mathbf{x}, \mathbf{y}, t);$$

- Flow rule

$$\dot{\gamma}^{s,0}(\mathbf{x}, \mathbf{y}, t) = \dot{\gamma}_0 \left(\frac{|\tau^{s,0}(\mathbf{x}, \mathbf{y}, t)|}{g^{s,0}(\mathbf{x}, \mathbf{y}, t)} \right)^{\frac{1}{m}} \text{sgn}(\tau^{s,0}(\mathbf{x}, \mathbf{y}, t));$$

- Hardening law

$$\dot{g}^{s,0}(\mathbf{x}, \mathbf{y}, t) = h_0 \left(\frac{g_{sa}^{s,0}(\mathbf{x}, \mathbf{y}, t) - g^{s,0}(\mathbf{x}, \mathbf{y}, t)}{g_{sa}^{s,0}(\mathbf{x}, \mathbf{y}, t) - g_0^{s,0}(\mathbf{x}, \mathbf{y})} \right) \sum_{s=1}^N |\dot{\gamma}^{s,0}(\mathbf{x}, \mathbf{y}, t)|;$$

$$g_{sa}^{s,0} = g_{sa,0}^s \left(\sum_{s=1}^N \frac{|\dot{\gamma}^{s,0}(\mathbf{x}, \mathbf{y}, t)|}{\dot{\gamma}_{s0}} \right)^m;$$

- Schmid law

$$\tau^{s,0}(\mathbf{x}, \mathbf{y}, t) = \sigma_{ij}^0(\mathbf{x}, \mathbf{y}, t) Z_{ij}^{s,0}(\mathbf{x}, \mathbf{y}, t);$$

- Θ -periodic boundary condition.

Remark 1. Theoretically, it is still necessary to investigate the equivalency of the kinematics and equilibrium equations between undeformed and deformed configurations for both macro- and micro-scale. This task is trivial once the mapping functions are known. One can obtain the relation between the stress measures (e.g., first Piola-Kirchoff stress \mathbf{P} and Cauchy stress $\boldsymbol{\sigma}$) and the strain measures (e.g., deformation gradient \mathbf{F} and rate of deformation tensor \mathbf{D}) in the two configura-

tions, which is essentially the equivalency of kinematics, and can be further used to demonstrate the equivalency of the equilibrium equations.

4. Model order reduction of the microscale problem

The microscale problem defined in Box II can be directly evaluated numerically (e.g., using the finite element method), however this may be computational expensive when the microstructure is complicated and needs intensive meshing to resolve its microstructure features properly. In this section, a reduced order model is formulated for the microscale problem. In what follows, the superscript 0 that indicates the leading order term in asymptotic or Taylor Series expansions are omitted from field variables for simplicity of presentation.

4.1. Linearization of the constitutive equations

Substituting the slip evolution (Eqs. (3.25)) and the Schmid law ((Eq. 3.26)) into Eq. (3.23) and rearranging the terms yield

$$D_{ij} = M_{ijkl}(\boldsymbol{\sigma}) \sigma_{kl} \quad (4.1)$$

in which the viscosity tensor \mathbf{M} is defined as

$$M_{ijkl}(\boldsymbol{\sigma}) = \dot{\gamma} \sum_{s=1}^N \left[\text{sym}(Z_{ij}^s) \frac{\text{sym}(Z_{kl}^s)}{g^s} \left(\frac{|\text{sym}(Z_{mn}^s) \sigma_{mnl}|}{g^s} \right)^{\frac{1}{m}-1} \right] \quad (4.2)$$

Equation (4.1) expresses the constitutive behavior in the form of a nonlinear, anisotropic, stress dependent non-Newtonian and incompressible fluid. The nonlinear stress-dependence of the viscosity tensor is clear since the slip system strength is also stress-dependent. Incompressibility emanates from the Schmid tensors, where the slip system normal and slip direction are always orthogonal to each other (i.e., $Z_{ii}^s = 0$). It is also clear from Eq. (4.2) that the viscosity tensor has major symmetry (i.e., $M_{ijkl} = M_{klij}$).

We proceed with a two-term Taylor Series approximation for $\mathbf{M}(\boldsymbol{\sigma})$ around a stress state $\hat{\boldsymbol{\sigma}}$

$$M_{ijkl}(\boldsymbol{\sigma}) = M_{ijkl}(\hat{\boldsymbol{\sigma}}) + \left. \frac{dM_{ijkl}}{d\sigma_{mn}} \right|_{\sigma=\hat{\boldsymbol{\sigma}}} (\sigma_{mn} - \hat{\sigma}_{mn}) \quad (4.3)$$

From a computational viewpoint, accuracy of the ensuing computations rely on choosing an appropriate stress point, $\hat{\boldsymbol{\sigma}}$, from which the Taylor Series approximation is made. The choice employed in this study is discussed in Section 5. Substituting Eq. (4.3) into Eq. (4.1), and rearranging the terms results in the following alternative form for the constitutive equation

$$\sigma_{ij} = L_{ijkl} (D_{kl} - \mu_{kl}) \quad (4.4)$$

where the fluidity tensor \mathbf{L} is defined as the inverse of viscosity tensor ($\mathbf{M}(\hat{\boldsymbol{\sigma}})^{-1}$), and $\boldsymbol{\mu}$ is the first order correction to the rate of deformation predicted by the stress state, $\hat{\boldsymbol{\sigma}}$

$$\mu_{ij} = \left. \frac{dM_{ijkl}}{d\sigma_{mn}} \right|_{\sigma=\hat{\boldsymbol{\sigma}}} (\sigma_{mn} - \hat{\sigma}_{mn}) \sigma_{kl} \quad (4.5)$$

Substituting Eqs. (3.17) and (3.19) to Eq. (4.4)

$$\sigma_{ij} = L_{ijkl} \left(\bar{D}_{kl} + v_{(k,y_l)}^1 - \mu_{kl} \right) \quad (4.6)$$

Combining Eq. (4.6) with Eq. (3.31), the microscopic equilibrium equation Eq. (3.31) is written as

$$\left[L_{ijkl} \left(\bar{D}_{kl} + v_{(k,y_l)}^1 - \mu_{kl} \right) \right]_{,yj} = 0 \quad (4.7)$$

Remark 2. One novelty of the present formulation is the linearization of the constitutive equation with a two-term Taylor Series expansion to provide higher order accuracy to the approximation of viscosity tensor \mathbf{M} . When the rate sensitivity parameter m is small (or $\frac{1}{m}$ is large), the extra term can stabilize the formulation and reduce the computational effort by keeping a relatively coarse time discretization. One may resort to even higher order expansions when the material is highly rate-sensitive, where m is a very small number.

4.2. Reduced-basis representation

The microscopic equilibrium equation derived above is similar in form to that used in the small-strain EHM theory [19, 27]. This similarity allows us to employ the principles of EHM to reduce the order of the microscale problem. The form of the microscale equation in small-strain EHM is due to the additive split of the strain tensor, and $\boldsymbol{\mu}$ corresponds to inelastic strains. The current formulation does not employ additive split, and $\boldsymbol{\mu}$ corresponds to the first order correction to the deformation rate tensor. Despite the difference in its physical meaning, the proposed formulation considers $\boldsymbol{\mu}$ as an eigen-field, similar to the eigenstrain treatment of $\boldsymbol{\mu}$ in small-strain EHM. Three additional differences set apart the current formulation from previous formulations: (1) the microscale equilibrium equation is defined at the current frame; (2) the macroscale “force function”, $\bar{\mathbf{D}}$ and $\boldsymbol{\mu}$ are rate quantities; and (3) the fluidity tensor, \mathbf{L} is a function of stress state, and hence not constant (unlike small-strain EHM, where the corresponding moduli tensor is constant).

We proceed with the following decomposition for the microscopic velocity field

$$v_i^1(\mathbf{x}, \mathbf{y}, t) = H_{ikl}(\mathbf{x}, \mathbf{y}, t) \bar{D}_{kl}(\mathbf{x}, t) + \int_{\Theta} h_{ikl}(\mathbf{x}, \mathbf{y}, \hat{\mathbf{y}}, t) \mu_{kl}(\mathbf{x}, \hat{\mathbf{y}}, t) d\hat{\mathbf{y}} \quad (4.8)$$

where \mathbf{H} and \mathbf{h} denote influence functions. The first term on the right hand side of Eq. (4.8) is an extension of the separation of variables principle employed in the classical linear elastic computational homogenization method [59]. The second term is obtained by the Green’s function approach, where the term $\boldsymbol{\mu}$ is viewed as the spatially varying “force” acting on the deformed frame of the microstructure domain.

Substituting Eq. (4.8) into the microscopic equilibrium equation (Eq. (4.7)) yields

$$\left\{ L_{ijkl}(\mathbf{x}, \mathbf{y}, t) \left[A_{klmn}(\mathbf{x}, \mathbf{y}, t) \bar{D}_{mn}(\mathbf{x}, t) + \int_{\Theta} a_{klmn}(\mathbf{x}, \mathbf{y}, \hat{\mathbf{y}}, t) \mu_{mn}(\mathbf{x}, \hat{\mathbf{y}}, t) d\hat{\mathbf{y}} \right] \right\}_{,yj} = 0 \quad (4.9)$$

where,

$$A_{klmn}(\mathbf{x}, \mathbf{y}, t) = G_{klmn}(\mathbf{x}, \mathbf{y}, t) + I_{klmn} \quad (4.10)$$

$$a_{klmn}(\mathbf{x}, \mathbf{y}, \hat{\mathbf{y}}, t) = g_{klmn}(\mathbf{x}, \mathbf{y}, \hat{\mathbf{y}}, t) - I_{klmn} \delta(\mathbf{y} - \hat{\mathbf{y}}) \quad (4.11)$$

with \mathbf{I} as the fourth order identity tensor and δ is the Dirac delta function. The polarization functions are defined as

$$G_{klmn}(\mathbf{x}, \mathbf{y}, t) = H_{(k,y)mn}(\mathbf{x}, \mathbf{y}, t) \quad (4.12)$$

$$g_{klmn}(\mathbf{x}, \mathbf{y}, \hat{\mathbf{y}}, t) = h_{(k,y)mn}(\mathbf{x}, \mathbf{y}, \hat{\mathbf{y}}, t) \quad (4.13)$$

We proceed by introducing the following discretizations for $\boldsymbol{\mu}$ and $\boldsymbol{\sigma}$

$$\mu_{ij}(\mathbf{x}, \mathbf{y}, t) = \sum_{\alpha=1}^n N^{(\alpha)}(\mathbf{y}) \mu_{ij}^{(\alpha)}(\mathbf{x}, t) \quad (4.14)$$

$$\sigma_{ij}(\mathbf{x}, \mathbf{y}, t) = \sum_{\alpha=1}^n N^{(\alpha)}(\mathbf{y}) \sigma_{ij}^{(\alpha)}(\mathbf{x}, t) \quad (4.15)$$

where $n \geq n_{\text{grain}}$ is an integer that indicates the order of the resulting reduced order model, n_{grain} is the number of grains within the CV, $N^{(\alpha)}$ is the reduced order shape function, $\boldsymbol{\mu}^{(\alpha)}$ and $\boldsymbol{\sigma}^{(\alpha)}$ are the nonlocal eigen-deformation rate and stress coefficients, respectively. The nonlocal coefficients are expressed in terms of nonlocal weight functions as

$$\mu_{ij}^{(\alpha)}(\mathbf{x}, t) = \int_{\Theta} \psi^{(\alpha)}(\mathbf{y}) \mu_{ij}(\mathbf{x}, \mathbf{y}, t) d\mathbf{y} \quad (4.16)$$

$$\sigma_{ij}^{(\alpha)}(\mathbf{x}, t) = \int_{\Theta} \psi^{(\alpha)}(\mathbf{y}) \sigma_{ij}(\mathbf{x}, \mathbf{y}, t) d\mathbf{y} \quad (4.17)$$

where the nonlocal weight functions satisfy[27]

$$\psi^{(\alpha)}(\mathbf{y}) \geq 0; \quad \int_{\Theta} \psi^{(\alpha)}(\mathbf{y}) d\mathbf{y} = 1; \quad \int_{\Theta} \psi^{(\alpha)}(\mathbf{y}) N^{(\beta)}(\mathbf{y}) d\mathbf{y} = \delta^{(\alpha\beta)} \quad (4.18)$$

in which $\delta^{(\alpha\beta)}$ is the Kronecker delta.

Substituting Eq. (4.9) into Eq. (3.17) with $k = 0$, we have

$$D_{ij}(\mathbf{x}, \mathbf{y}, t) = A_{ijkl}(\mathbf{x}, \mathbf{y}, t) \bar{D}_{kl}(\mathbf{x}, t) + \int_{\Theta} g_{ijkl}(\mathbf{x}, \mathbf{y}, \hat{\mathbf{y}}, t) \mu_{kl}(\mathbf{x}, \hat{\mathbf{y}}) d\hat{\mathbf{y}} \quad (4.19)$$

Substituting Eq. (4.14) into Eq. (4.19), premultiplying the resulting equation with $\psi^{(\alpha)}$ and integrating over the CV domain yield

$$D_{ij}^{(\beta)}(\mathbf{x}, t) - \sum_{\alpha=1}^n P_{ijkl}^{(\beta\alpha)}(\mathbf{x}, t) \mu_{kl}^{(\alpha)}(\mathbf{x}, t) = A_{ijkl}^{(\beta)}(\mathbf{x}, t) \bar{D}_{kl}(\mathbf{x}, t) \quad (4.20)$$

in which $\mathbf{P}^{(\beta\alpha)}$ and $\mathbf{A}^{(\beta)}$ are the coefficient tensors expressed as functions of the polarization tensors as

$$P_{ijkl}^{(\beta\alpha)}(\mathbf{x}, t) = \int_{\Theta} \int_{\Theta} \psi^{(\beta)}(\mathbf{y}) N^{(\alpha)}(\hat{\mathbf{y}}) g_{ijkl}(\mathbf{x}, \mathbf{y}, \hat{\mathbf{y}}, t) dy d\hat{\mathbf{y}} \quad (4.21)$$

$$A_{ijkl}^{(\beta)}(\mathbf{x}, t) = \int_{\Theta} \psi^{(\beta)}(\mathbf{y}) A_{ijkl}(\mathbf{x}, \mathbf{y}, t) dy \quad (4.22)$$

and,

$$D_{ij}^{(\beta)}(\mathbf{x}, t) := \int_{\Theta} \psi^{(\beta)}(\mathbf{y}) D_{ij}^0(\mathbf{x}, \mathbf{y}, t) dy \quad (4.23)$$

Applying the same operation for the spin tensor, we obtain

$$W_{ij}^{(\beta)}(\mathbf{x}, t) = \bar{W}_{ij}(\mathbf{x}, t) + S_{ijkl}^{(\beta)}(\mathbf{x}, t) \bar{D}_{kl}(\mathbf{x}, t) + \sum_{\alpha=1}^n T_{ijkl}^{(\beta\alpha)}(\mathbf{x}, t) \mu_{kl}^{(\alpha)}(\mathbf{x}, t) \quad (4.24)$$

where $\mathbf{T}^{(\beta\alpha)}$ and $\mathbf{S}^{(\beta)}$ are two additional coefficient tensors that emanate from the skew part of the influence function gradient over the microscopic domain.

$$T_{ijkl}^{(\beta\alpha)}(\mathbf{x}, t) = \int_{\Theta} \psi^{(\beta)}(\mathbf{y}) h_{\langle i, y_j \rangle kl}^{(\alpha)}(\mathbf{x}, \mathbf{y}, t) dy \quad (4.25)$$

$$S_{ijkl}^{(\beta)}(\mathbf{x}, t) = \int_{\Theta} \psi^{(\beta)}(\mathbf{y}) H_{\langle i, y_j \rangle kl}(\mathbf{x}, \mathbf{y}, t) dy \quad (4.26)$$

We turn our attention to expressing the constitutive law as a function of the reduced order model variables. We begin by rewriting Eq. (4.4) as

$$D_{ij}(\mathbf{x}, \mathbf{y}, t) - \mu_{ij}(\mathbf{x}, \mathbf{y}, t) = M_{ijkl} \Big|_{\sigma=\hat{\sigma}} \sigma_{kl}(\mathbf{x}, \mathbf{y}, t) \quad (4.27)$$

Substituting Eq. (4.17) into Eq. (4.27), premultiplying it with $\psi^{(\alpha)}$, and integrating over the RVE domain yield

$$D_{ij}^{(\beta)}(\mathbf{x}, t) = \mu_{ij}^{(\beta)}(\mathbf{x}, t) + \sum_{\alpha=1}^n M_{ijkl}^{(\beta\alpha)} \Big|_{\sigma^{(\alpha)}=\hat{\sigma}^{(\alpha)}} \sigma_{kl}^{(\alpha)}(\mathbf{x}, t) \quad (4.28)$$

where $\hat{\sigma}^{(\alpha)}$ denotes the approximated stress for part α from the Taylor Series expansion, and $\mathbf{M}^{(\beta\alpha)}$ is

$$M_{ijkl}^{(\beta\alpha)}(\mathbf{x}, t) = \int_{\Theta} \psi^{(\beta)}(\mathbf{y}) M_{ijkl}(\mathbf{x}, \mathbf{y}, t) N^{(\alpha)}(\mathbf{y}) dy \quad (4.29)$$

Combining Eq. (4.20) and Eq. (4.28) results in the expression of the constitutive equation in terms of the reduced order model unknowns (i.e., $\sigma^{(\alpha)}$ and $\mu^{(\alpha)}$)

$$\sum_{\alpha=1}^n M_{ijkl}^{(\beta\alpha)} \Big|_{\sigma^{(\alpha)}=\hat{\sigma}^{(\alpha)}} \sigma_{kl}^{(\alpha)}(\mathbf{x}, t) - \sum_{\alpha=1}^n \left[P_{ijkl}^{(\beta\alpha)}(\mathbf{x}, t) - \delta^{(\alpha\beta)} I_{ijkl} \right] \mu_{kl}^{(\alpha)}(\mathbf{x}, t) = A_{ijkl}^{(\beta)}(\mathbf{x}, t) \bar{D}_{kl}(\mathbf{x}, t) \quad (4.30)$$

The coefficient tensors $\mathbf{M}^{(\beta\alpha)}$, $\mathbf{P}^{(\beta\alpha)}$ and $\mathbf{A}^{(\beta)}$ provide the microstructural information to the resulting model.

The choice of shape functions $N^{(\alpha)}$ directly affect the efficiency and accuracy of the resulting reduced order model [29]. In this manuscript, we employ piecewise constant functions as the shape functions [60]

$$N^{(\alpha)}(\mathbf{y}) = \begin{cases} 1 & \mathbf{y} \in \Theta^{(\alpha)} \\ 0 & \mathbf{y} \notin \Theta^{(\alpha)} \end{cases} \quad (4.31)$$

$$\psi^{(\alpha)}(\mathbf{y}) = \frac{1}{|\Theta^{(\alpha)}|} N^{(\alpha)}(\mathbf{y}) \quad (4.32)$$

where $\Theta^{(\alpha)}$ denotes a part of the CV. The domain partitioning is performed such that the parts are non-overlapping i.e., $\Theta = \bigcup_{\alpha=1}^n \Theta^{(\alpha)}$ and $\Theta^{(\alpha)} \cap \Theta^{(\beta)} = \emptyset$ for $\alpha \neq \beta$, and each part contains a uniform piece of material (e.g., a grain or a part of a grain with constant orientation). As a result, the coarsest basis for a polycrystalline material is a one-part-per-grain reduced order model. In view of this selection, the material parameters and grain orientation associated with each part $\Theta^{(\alpha)}$ is spatially constant (e.g., $\mathbf{Z}^s(\mathbf{x}, \mathbf{y}, t) = \mathbf{Z}^{s(\alpha)}(\mathbf{x}, t)$ when $\mathbf{y} \in \Theta^{(\alpha)}$). The shape and weight function selection strategy used in this work is further explained in [27, 29].

Premultiplying Eq. (3.26) with $\psi^{(\alpha)}$ and integrating over the CV domain yield:

$$\tau^{s(\alpha)}(\mathbf{x}, t) = \sigma_{ij}^{s(\alpha)}(\mathbf{x}, t) Z_{ij}^{s(\alpha)}(\mathbf{x}, t) \quad (4.33)$$

where $\tau^{s(\alpha)}$ is the part-average resolved shear stress of the s^{th} slip system, and $\mathbf{Z}^{s(\alpha)}$ denotes the Schmid tensor associated with part α .

Noting that the resolved shear stress in the reduced order model is piecewise uniform by the above argument, the slip and hardening evolve in a piecewise uniform fashion as well. The hardening evolution equations are therefore expressed in terms of part-average quantities

$$\dot{\gamma}^{s(\alpha)}(\mathbf{x}, t) = \dot{\gamma}_0 \left(\frac{|\tau^{s(\alpha)}(\mathbf{x}, t)|}{g^{s(\alpha)}(\mathbf{x}, t)} \right)^{\frac{1}{m}} \text{sgn}(\tau^{s(\alpha)}(\mathbf{x}, t)) \quad (4.34)$$

$$\dot{g}^{s(\alpha)}(\mathbf{x}, t) = h_0 \left(\frac{g_{sa}^{s(\alpha)}(\mathbf{x}, t) - g^{s(\alpha)}(\mathbf{x}, t)}{g_{sa}^{s(\alpha)}(\mathbf{x}, t) - g_0^{s(\alpha)}(\mathbf{x})} \right) \sum_{s=1}^N |\dot{\gamma}^{s(\alpha)}(\mathbf{x}, t)| \quad (4.35)$$

where $\dot{\gamma}^{s(\alpha)}$, $g^{s(\alpha)}$ and $g_{sa}^{s(\alpha)}$ are the part-average slip rate, slip system strength and saturation shear stress of the s^{th} slip system, respectively.

Premultiplying Eq. (3.24) with $\psi^{(\alpha)}$, integrating over the CV domain, and since both Schmid tensor and slip rate are piecewise uniform, the part-average plastic spin is obtained as

$$W_{ij}^{P(\alpha)}(\mathbf{x}, t) = \dot{\gamma}_0 \sum_{s=1}^N \text{skew} \left(Z_{ij}^{s(\alpha)} \right) \left(\frac{|\tau^{s(\alpha)}(\mathbf{x}, t)|}{g^{s(\alpha)}(\mathbf{x}, t)} \right)^{\frac{1}{m}} \text{sgn}(\tau^{s(\alpha)}(\mathbf{x}, t)) \quad (4.36)$$

Employing the same operation for Eq. (3.30), the evolution of the rotation tensor is written in a

part-wise fashion as

$$\dot{R}_{ij}^{(\alpha)} = \left(W_{im}^{(\alpha)} - W_{im}^{p(\alpha)} \right) R_{mj}^{(\alpha)} \quad (4.37)$$

where $\mathbf{R}^{(\alpha)} = \int_{\Theta} \psi^{(\alpha)} \mathbf{R}^0 d\mathbf{y}$.

The non-overlapping and piecewise constant choice for the shape and weight functions, when applied to Eq. (4.29) leads to

$$M_{ijkl}^{(\alpha\beta)} = 0 \quad \text{if } \alpha \neq \beta \quad (4.38)$$

Substituting Eq. (4.2) into Eq. (4.29), noting that the Schmid tensor, slip system strength and Cauchy stress are spatially constant within each part $\Theta^{(\alpha)}$

$$M_{ijkl}^{(\alpha\alpha)} = \dot{\gamma}_0 \sum_{s=1}^N \left[\text{sym} \left(Z_{ij}^{s(\alpha)} \right) \frac{\text{sym} \left(Z_{kl}^{s(\alpha)} \right)}{g^{s(\alpha)}} \left(\frac{\left| \text{sym} \left(Z_{mn}^{s(\alpha)} \right) \sigma_{mn}^{(\alpha)} \right|^{\frac{1}{m}-1}}{g^{s(\alpha)}} \right) \right] \quad (4.39)$$

Considering Eq. (4.5) and expanding the total derivative, the eigen-deformation rate $\boldsymbol{\mu}$ is written as

$$\mu_{ij} = \frac{\partial M_{ijkl}}{\partial \sigma_{mn}} \Big|_{\sigma=\hat{\sigma}} (\sigma_{kl} - \hat{\sigma}_{kl}) \sigma_{mn} + \left(\frac{\partial M_{ijkl}}{\partial g^s} \frac{\partial g^s}{\partial \sigma_{mn}} \right) \Big|_{\sigma=\hat{\sigma}} (\sigma_{kl} - \hat{\sigma}_{kl}) \sigma_{mn} \quad (4.40)$$

where the contribution of the Schmid tensor is not included. The reason is that the texture evolution is relatively slow compared to stress and slip system strength, of which the influence is negligible especially when the second order term of Taylor Series expansion is considered. In order to eliminate the complexity induced by the term $\partial g^s / \partial \sigma$, we use a two-term Taylor Series expansion for $g^s(\boldsymbol{\sigma})$ around $\hat{\boldsymbol{\sigma}}$ as

$$g^s(\boldsymbol{\sigma}) = g^s(\hat{\boldsymbol{\sigma}}) + \frac{\partial g^s}{\partial \sigma_{ij}} \Big|_{\sigma=\hat{\sigma}} (\sigma_{ij} - \hat{\sigma}_{ij}) \quad (4.41)$$

Substituting Eq. (4.41) into Eq. (4.40) yields

$$\mu_{ij} = \frac{\partial M_{ijkl}}{\partial \sigma_{mn}} \Big|_{\sigma=\hat{\sigma}} (\sigma_{kl} - \hat{\sigma}_{kl}) \sigma_{mn} + \frac{\partial M_{ijkl}}{\partial g^s} \Big|_{\sigma=\hat{\sigma}} (g^s - \hat{g}^s) \sigma_{kl} \quad (4.42)$$

in which $\hat{g}^s = g^s(\hat{\boldsymbol{\sigma}})$.

Using Eq. (4.42), it is straightforward to see that the part-average eigen-deformation rate for part α is

$$\mu_{ij}^{(\alpha)} = \frac{\partial M_{ijkl}^{(\alpha\alpha)}}{\partial \sigma_{mn}^{(\alpha)}} \Big|_{\sigma^{(\alpha)}=\hat{\sigma}^{(\alpha)}} (\sigma_{kl}^{(\alpha)} - \hat{\sigma}_{kl}^{(\alpha)}) \sigma_{mn}^{(\alpha)} + \frac{\partial M_{ijkl}^{(\alpha\alpha)}}{\partial g^{s(\alpha)}} \Big|_{\sigma^{(\alpha)}=\hat{\sigma}^{(\alpha)}} (g^{s(\alpha)} - \hat{g}^{s(\alpha)}) \sigma_{kl}^{(\alpha)} \quad (4.43)$$

Box III summarizes the reduced order microscale problem. Provided that n is small, the reduced order model is significantly more efficient compared with the evolution of the original microscale BVP described in Box II. The unknowns of the reduced order model are the part-average stress, slip system strength and textures.

Box III. Reconstructed microscale problem

Given: part-wise parameters $\mathbf{n}^{s(\alpha)}$, $\mathbf{m}^{s(\alpha)}$, $g_{sa}^{s(\alpha)}$, $\dot{\gamma}_0^{s(\alpha)}$, $h_0^{(\alpha)}$, $g_{s0}^{s(\alpha)}$, $\dot{\gamma}_{s0}^{(\alpha)}$, the macroscale rate of deformation tensor $\bar{\mathbf{D}}$ computed from deformation gradient $\bar{\mathbf{F}}$ and its increment $\Delta\bar{\mathbf{F}}$ within time increment Δt . Compute coefficient tensors $\mathbf{M}^{(\alpha\beta)}$, $\mathbf{P}^{(\beta\alpha)}$, $\mathbf{A}^{(\beta)}$, $\mathbf{T}^{(\beta\alpha)}$ and $\mathbf{S}^{(\beta)}$ at time t .

Find: macroscale stress $\bar{\boldsymbol{\sigma}}$ by solving

- Stress update

$$\sum_{\alpha=1}^n M_{ijkl}^{(\alpha\beta)} \Big|_{\boldsymbol{\sigma}^{(\alpha)}=\hat{\boldsymbol{\sigma}}^{(\alpha)}} \sigma_{kl}^{(\alpha)}(\mathbf{x}, t) - \sum_{\alpha=1}^n \left[P_{ijkl}^{(\alpha\beta)}(\mathbf{x}, t) - \delta^{(\alpha\beta)} I_{ijkl} \right] \mu_{kl}^{(\alpha)}(\mathbf{x}, t) = A_{ijkl}^{(\beta)}(\mathbf{x}, t) \bar{D}_{kl}(\mathbf{x}, t);$$

$$\mu_{ij}^{(\alpha)} = \frac{\partial M_{ijkl}^{(\alpha\alpha)}}{\partial \sigma_{mn}^{(\alpha)}} \Big|_{\boldsymbol{\sigma}^{(\alpha)}=\hat{\boldsymbol{\sigma}}^{(\alpha)}} (\sigma_{kl}^{(\alpha)} - \hat{\sigma}_{kl}^{(\alpha)}) \sigma_{mn}^{(\alpha)} + \frac{\partial M_{ijkl}^{(\alpha\alpha)}}{\partial g_{sa}^{s(\alpha)}} \Big|_{\boldsymbol{\sigma}^{(\alpha)}=\hat{\boldsymbol{\sigma}}^{(\alpha)}} (g_{sa}^{s(\alpha)} - \hat{g}_{sa}^{s(\alpha)}) \sigma_{kl}^{(\alpha)};$$

$$\bar{\sigma}_{ij}(\mathbf{x}, t) = \frac{1}{|\Theta|} \int_{\Theta} \sigma_{ij}^0(\mathbf{x}, \mathbf{y}, t) d\Theta; \quad \sigma_{ij}^0(\mathbf{x}, \mathbf{y}, t) = \sum_{\alpha=1}^n N^{(\alpha)}(\mathbf{y}) \sigma_{ij}^{(\alpha)}(\mathbf{x}, t).$$

- Slip system strength update

$$\dot{\gamma}^{s(\alpha)}(\mathbf{x}, t) = \dot{\gamma}_0 \left(\frac{|\tau^{s(\alpha)}(\mathbf{x}, t)|}{g^{s(\alpha)}(\mathbf{x}, t)} \right)^{\frac{1}{m}} \text{sgn}(\tau^{s(\alpha)}(\mathbf{x}, t));$$

$$\dot{g}^{s(\alpha)}(\mathbf{x}, t) = h_0 \left(\frac{g_{sa}^{s(\alpha)}(\mathbf{x}, t) - g^{s(\alpha)}(\mathbf{x}, t)}{g_{sa}^{s(\alpha)}(\mathbf{x}, t) - g_0^{s(\alpha)}(\mathbf{x})} \right) \sum_{s=1}^N |\dot{\gamma}^{s(\alpha)}(\mathbf{x}, t)|;$$

$$\tau^{s(\alpha)}(\mathbf{x}, t) = \sigma_{ij}^{(\alpha)}(\mathbf{x}, t) Z_{ij}^{s(\alpha)}(\mathbf{x}, t).$$

- Texture update

$$W_{ij}^{(\beta)}(\mathbf{x}, t) = \bar{W}_{ij}(\mathbf{x}, t) + S_{ijkl}^{(\beta)}(\mathbf{x}, t) \bar{D}_{kl}(\mathbf{x}, t) + \sum_{\alpha=1}^n T_{ijkl}^{(\beta\alpha)}(\mathbf{x}, t) \mu_{kl}^{(\alpha)}(\mathbf{x}, t);$$

$$W_{ij}^{P(\alpha)}(\mathbf{x}, t) = \dot{\gamma}_0 \sum_{s=1}^N \text{skew}(Z_{ij}^{s(\alpha)}) \left(\frac{|\tau^{s(\alpha)}(\mathbf{x}, t)|}{g^{s(\alpha)}(\mathbf{x}, t)} \right)^{\frac{1}{m}} \text{sgn}(\tau^{s(\alpha)}(\mathbf{x}, t)).$$

4.3. Influence function problems

The influence functions associated with the macroscopic deformation gradient, $\bar{\mathbf{D}}$ and $\boldsymbol{\mu}$ vary as a function of time and both spatial scales. Time and macroscale position dependence of the

influence functions are because the microscale problem is posed on the deformed configuration, and the stress-dependence of the fluidity tensor. This is in contrast with the small-strain EHM formulation, where the influence functions are time invariant, and does not depend on the macroscale coordinates provided that the entire structural domain is defined by the same CV.

The governing equation for the influence function, \mathbf{H} is obtained from Eq. (4.9) considering the case when the eigendeformation rate (i.e., the second order effects) are negligible

$$\left\{ L_{ijmn}(\mathbf{x}, \mathbf{y}, t) \left[H_{(m,y_n)kl}(\mathbf{x}, \mathbf{y}, t) + I_{mnkl} \right] \right\}_{,y_j} = 0 \quad (4.44)$$

Equation (4.44) along with periodic boundary conditions form the first order influence function problem.

Substituting the eigen-deformation rate discretization (Eq. (4.16)) and Eq. (4.44) into Eq. (4.9), we obtain

$$\left\{ L_{ijmn}(\mathbf{x}, \mathbf{y}, t) \left[h_{(m,y_n)kl}^{(\alpha)}(\mathbf{x}, \mathbf{y}, t) - I_{mnkl} N^{(\alpha)}(\mathbf{y}) \right] \right\}_{,y_j} = 0 \quad (4.45)$$

where $\mathbf{h}^{(\alpha)}$ is defined as

$$h_{ikl}^{(\alpha)}(\mathbf{x}, \mathbf{y}, t) = \int_{\Theta} N^{(\alpha)}(\mathbf{y}) h_{ikl}(\mathbf{x}, \mathbf{y}, \hat{\mathbf{y}}, t) d\hat{\mathbf{y}} \quad (4.46)$$

Equation (4.45) along with periodic boundary conditions form the second order influence function problem. Equations (4.44) and (4.45) are well-posed linear influence function problems that are evaluated using the finite element method (see for small deformation analogs [27, 59]).

Substitute Eq. (4.46) into Eq. (4.21), it is possible to directly evaluate $\mathbf{P}^{(\beta\alpha)}$ using the part-wise eigen-deformation rate influence function as [27]

$$P_{ijkl}^{(\beta\alpha)}(\mathbf{x}, t) = \int_{\Theta} \psi^{(\beta)}(\mathbf{y}) h_{(i,y_j)kl}^{(\alpha)}(\mathbf{x}, \mathbf{y}, t) d\mathbf{y} \quad (4.47)$$

5. Numerical implementation

The macroscale problem summarized in Box I combined with the reduced order microscale problem summarized in Box III constitute the multiscale reduced order system. At a given macroscopic material point, the evolution of the reduced order microscale problem serves as the constitutive update to compute the macroscopic stress tensor. One important consideration in the straightforward implementation of the coupled multiscale system is that the influence functions, \mathbf{H} and $\mathbf{h}^{(\alpha)}$, and hence the coefficient tensors, $\mathbf{A}^{(\alpha)}$, $\mathbf{P}^{(\beta\alpha)}$, $\mathbf{S}^{(\alpha)}$ and $\mathbf{T}^{(\beta\alpha)}$ are state-dependent and require recomputation at each macroscopic material point and each macroscopic increment. While the evolution of the reduced order microscale problem (with low n) is efficient, the computation of the coefficient tensors is not. As demonstrated by the numerical verification example below, the coefficient tensors exhibit a mild evolution as a function of deformation, where the macroscopic deformation rate is relatively constant. The coefficient tensors are primarily dictated by the loading rate. In view of this observation, we employ a computationally efficient implementation scheme that does not rely on frequent coefficient tensors recomputations.

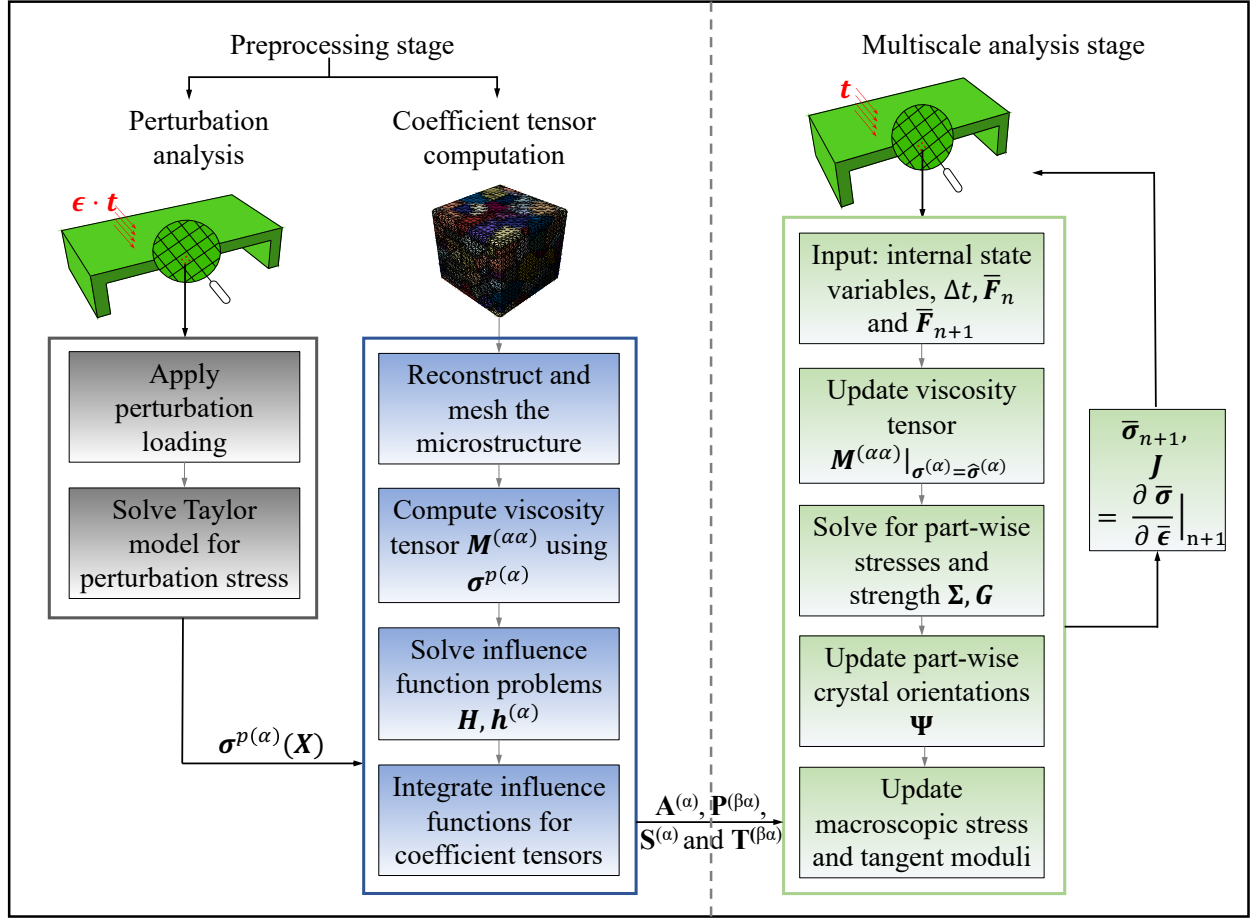


Figure 4: Overview of the implementation strategy

Figure 4 illustrates the overview of the proposed implementation strategy. The present strategy only requires computing the coefficient tensors once at each macroscopic point. The multiscale system is evaluated in two stages: (1) preprocessing stage and (2) multiscale analysis stage.

5.1. Preprocessing stage

The preprocessing stage is performed in two steps: (1a) perturbation analysis and (1b) coefficient tensor computation. The purpose of the perturbation analysis step is to compute a reasonable and non-zero initial guess for the macroscopic stress state to compute the coefficient tensors and initiate the reduced order model. A zero initial guess results in a trivial viscosity tensor and hence trivial coefficient tensors (see Eq. 5.1). In this step, the macroscopic domain is subjected to the same loading condition that would be applied in the multiscale analysis stage but with much smaller magnitude (i.e., $0 < \epsilon \ll 1$). The problem is evaluated using the Taylor model, where each grain within the microstructure domain is subjected to the same macroscopic deformation rate [16]. While it is possible to obtain the coefficient tensors directly using the reduced order model, our investigations indicated occasional convergence difficulty for poor choices of initial guess of stress states, and require multiple coefficient tensor computations during the iterations.

The Taylor model provides a computational efficient way to estimate the viscosity tensor with a microstructure without resorting to complex computations. At the end of the perturbation step, the perturbation stress field $\sigma^{p(\alpha)}(\mathbf{X})$ is obtained.

In the coefficient tensor computation step, firstly, the microstructure is constructed and meshed. At each quadrature point, the viscosity tensor is computed as

$$M_{ijkl}(\sigma^{p(\alpha)}) = \dot{\gamma}_0 \sum_{s=1}^N \left[\text{sym}(Z_{ij}^{s(\alpha)}) \frac{\text{sym}(Z_{kl}^{s(\alpha)})}{g^{s(\alpha)}} \left(\frac{|\text{sym}(Z_{mn}^{s(\alpha)}) \sigma_{mn}^{p(\alpha)}|}{g^{s(\alpha)}} \right)^{\frac{1}{m}-1} \right] + \kappa \delta_{ij} \delta_{kl} \quad (5.1)$$

where κ is a very small positive number served as the penalty term, which is taken to be 1E-08 in our study, and δ is the Kronecker delta. Compared with Eq. (4.39), Eq. (5.1) includes a penalty term to account for the near rigid hydrostatic behavior. In the absence of the hydrostatic term, the viscosity tensor (i.e., Eq. (4.39)) is rank deficient and not invertible since it is a deviatoric tensor. Next, the influence function problems are solved (Eqs. (4.44) and (4.45)). The implementation details of solving the influence function problem can be found in [27]. The coefficient tensors are obtained through the integration of the influence functions over the microstructure domain.

Remark 3. In microstructures that are subjected to time varying strain rates, the effect of coefficient tensor evolution could be significant and consideration of time invariant coefficient tensors may not be valid. In such cases, the computational burden due to coefficient tensor recomputations could be decreased by considering an adaptive update procedure, where the frequency of coefficient tensor updates is dictated by the change in the strain rate. Such cases and optimal update strategies are out of the scope of the current study.

5.2. Multiscale analysis stage

In the multiscale analysis stage, the macroscale problem and the reduced order microscale problems are evaluated in a coupled fashion. The reduced order microscale problem is implemented as a local stress update procedure within the macroscale problem. The macroscale problem is evaluated using the nonlinear finite element approach with the Newton-Raphson scheme. The macroscopic stress update procedure is implemented as follows (Fig. 4). At each quadrature point, the driving force is the macroscopic strain rate $\bar{\mathbf{D}}$ (computed from deformation gradient $\bar{\mathbf{F}}$). At the beginning of each time increment, the first order approximation of the stress tensor in the Taylor series expansion is taken to be the stress field from last increment (i.e., $\hat{\sigma}_{n+1}^{(\alpha)} = \sigma_n^{(\alpha)}$), and the approximation of viscosity tensor $\mathbf{M}^{(\alpha\alpha)}|_{\sigma^{(\alpha)}=\hat{\sigma}^{(\alpha)}}$ is updated from the old state accordingly (Taylor model is used for the first increment to compute the initial state). Next, the microscale reduced order system of equations are solved for the part-wise stress, strength and crystal orientations using the coefficient tensors computed at the preprocessing stage. The macroscopic stress and tangent moduli then are updated and passed to the macroscale solver.

The reduced order system of microscale equations in Box III are three sets of coupled nonlinear equations with part-wise stresses $\sigma^{(\alpha)}$, strengths $g^{s(\alpha)}$ and orientations $\Psi^{(\alpha)}$ as unknowns. A staggered scheme is adopted to solve this system, in which the part-wise stress and part-wise slip system strengths are evaluated in a coupled but iterative manner. The orientations are updated once

the stresses and strengths are converged. The details of the evaluation of stress and slip system strength are similar to the procedure provided in [27]. In this section, we discuss the details of the texture update.

Expressing the orientation of part α using Euler angles $(\psi_1^{(\alpha)}, \phi^{(\alpha)}, \psi_2^{(\alpha)})$, $\mathbf{C}^{(\alpha)}$ indicates matrix representation of the rotation tensor in Kock's convention [11]. Superscript α is omitted in Eq. (5.2) for simplicity.

$$[\mathbf{C}^{(\alpha)}] = \begin{bmatrix} \cos \psi_1 \cos \psi_2 - \sin \psi_1 \cos \phi \sin \psi_2 & -\cos \psi_1 \sin \psi_2 - \sin \psi_1 \cos \phi \cos \psi_2 & \sin \psi_1 \sin \phi \\ \sin \psi_1 \cos \psi_2 + \cos \psi_1 \cos \phi \sin \psi_2 & -\sin \psi_1 \sin \psi_2 + \cos \psi_1 \cos \phi \cos \psi_2 & -\cos \psi_1 \sin \phi \\ \sin \psi_2 \sin \phi & \cos \psi_2 \sin \phi & \cos \phi \end{bmatrix} \quad (5.2)$$

Considering Eqs. (2.19)-(2.21) in a part-wise fashion, the Schmid tensor for part α to its initial value is

$$\mathbf{Z}^{s(\alpha)} = \mathbf{C}^{(\alpha)} \mathbf{Z}_0^{s(\alpha)} (\mathbf{C}^{(\alpha)})^T \quad (5.3)$$

$$\mathbf{C}^{(\alpha)} = \mathbf{R}^{(\alpha)} \mathbf{C}_0^{(\alpha)} \quad (5.4)$$

where $\mathbf{Z}_0^{s(\alpha)} = \mathbf{n}_0^{s(\alpha)} \otimes \mathbf{m}_0^{s(\alpha)}$ and $\mathbf{C}_0^{(\alpha)}$ is the initial orientation for part α . We adopt an exponential mapping suggested by Simo and Hughes [61] to update $\mathbf{R}^{(\alpha)}$ by

$$\mathbf{R}_{n+1}^{(\alpha)} = \exp(\Delta \mathbf{W}_{n+1}^{(\alpha)}) \mathbf{R}_n^{(\alpha)} \quad (5.5)$$

where

$$\Delta \mathbf{W}_{n+1}^{(\alpha)} = \Delta t_{n+1} (\dot{\mathbf{R}}^{(\alpha)} \mathbf{R}^{(\alpha)T})_{n+1} = \Delta t_{n+1} (\mathbf{W}_{n+1}^{(\alpha)} - \mathbf{W}_{n+1}^{P(\alpha)}) \quad (5.6)$$

6. Numerical verification

This section focuses on the verification of the proposed large deformation reduced order model (LROM) by comparison with CPFEM simulations (i.e., the reference model), in which the microstructure is fully resolved. Two sets of examples are studied to characterize the accuracy and efficiency of LROM. The first set of examples are single crystal simulations, in which a voided microstructure is employed. The second set of examples are on synthetic polycrystalline microstructures and enable the assessment of LROM capabilities in more complex morphologies. In both sets of examples, accuracy in terms of the overall stress-strain behavior, anisotropy, and texture evolution are investigated. For polycrystalline microstructures, the localized behaviors are also investigated.

The verification examples consider microstructures that consist of face centered cubic (FCC) crystals. All 12 $\{111\}\langle 111 \rangle$ slip systems are considered to be active in the simulations. The parameters of the constitutive model for the crystal used in the simulations are summarized in Table 1.

Table 1: Viscoplasticity parameters.

m	$\dot{\gamma}_0 (s^{-1})$	h_0 (Mpa)	g_0^s (Mpa)	$g_{sa,0}^s$ (Mpa)	m'	$\dot{\gamma}_{s0} (s^{-1})$
0.25	1.0	20.4	3.7	30.8	0.0	5.0×10^{10}

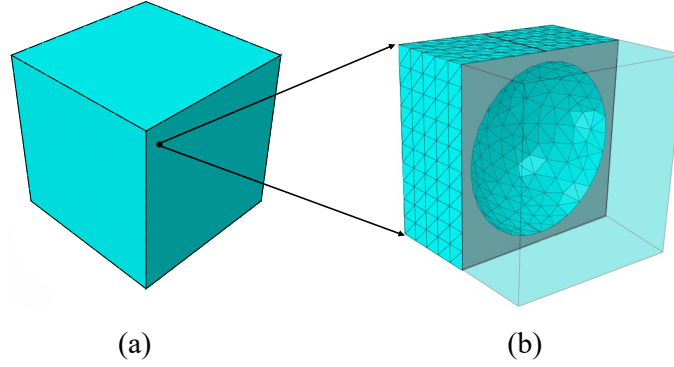


Figure 5: (a) macroscale discretization, (b) microscale geometry and discretization of a voided single crystal microstructure.

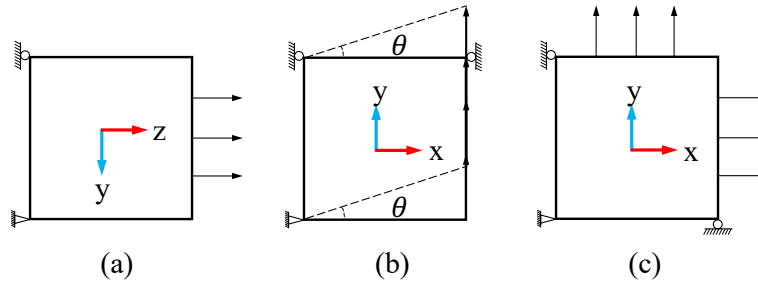


Figure 6: Schematic illustration of three boundary conditions: (a) uniaxial tension, (b) simple shear and (c) biaxial tension

Table 2: Orientations used in single crystal simulation, ψ_1 , ϕ and ψ_2 are Euler angles.

	orientation 1	orientation 2	orientation 3	orientation 4	orientation 5
$\psi_1(^{\circ})$	88.98	13.58	101.9	132.81	238.51
$\phi(^{\circ})$	124.12	153.68	145.03	105.72	61.10
$\psi_2(^{\circ})$	115.16	314.4	249.44	180.69	158.50

6.1. Voided single crystal simulations

Figure 5 (b) shows the geometry and discretization of the microstructure used in this example. A spherical void is included within the material microstructure. The finite element discretization of the reference CPFEM simulation consists of 5,707 tetrahedron elements. The LROM consists of a single part (i.e., $n=1$), where a single basis function is used to discretize the microstructure. A single trilinear eight-noded hexahedron element is used for the macroscopic discretization of the multiscale model (Fig. 5 (a)).

25 separate microstructures were tested by varying the void diameter and the crystal orientation: the void diameter varies from $0.5\mu\text{m}$ to $0.9\mu\text{m}$ (the edge length of the microstructure is $1\mu\text{m}$). 5 crystal orientations investigated are shown in Table 2. As shown in Fig. 6, three loading conditions are considered to evaluate the performance of the reduced order model for each simulation case: uniaxial tension, simple shear and biaxial tension (the 2D representation is for simplicity

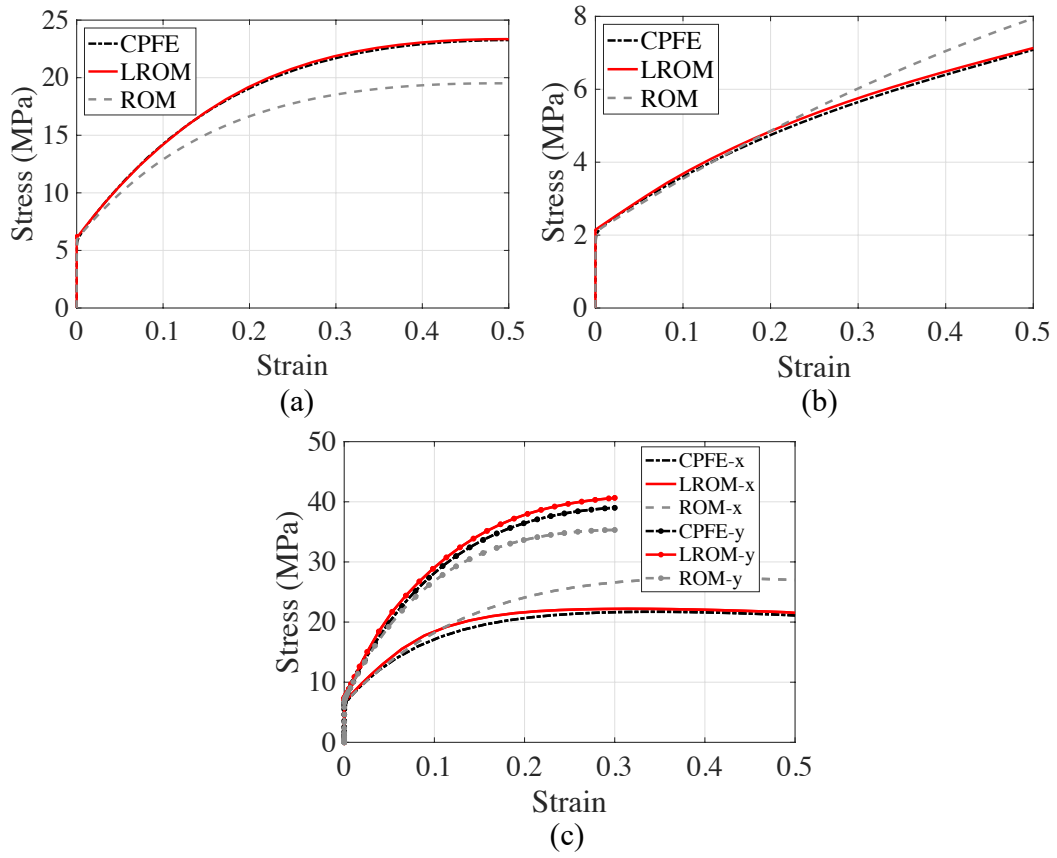


Figure 7: Overall stress-strain curves for voided RVE of diameter = $0.9 \mu\text{m}$ with orientation 1 subjected to (a) uniaxial tension, (b) simple shear and (c) biaxial tension.

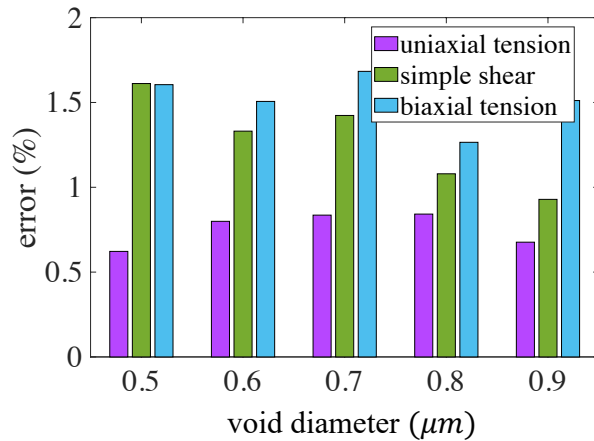


Figure 8: Overall stress approximation error of all simulations for voided single crystals

since no loading is applied in the third direction). The loading is strain controlled. 50% strain is applied at constant strain rate of $0.5/\text{s}$ for the uniaxial tension and the simple shear cases. In the

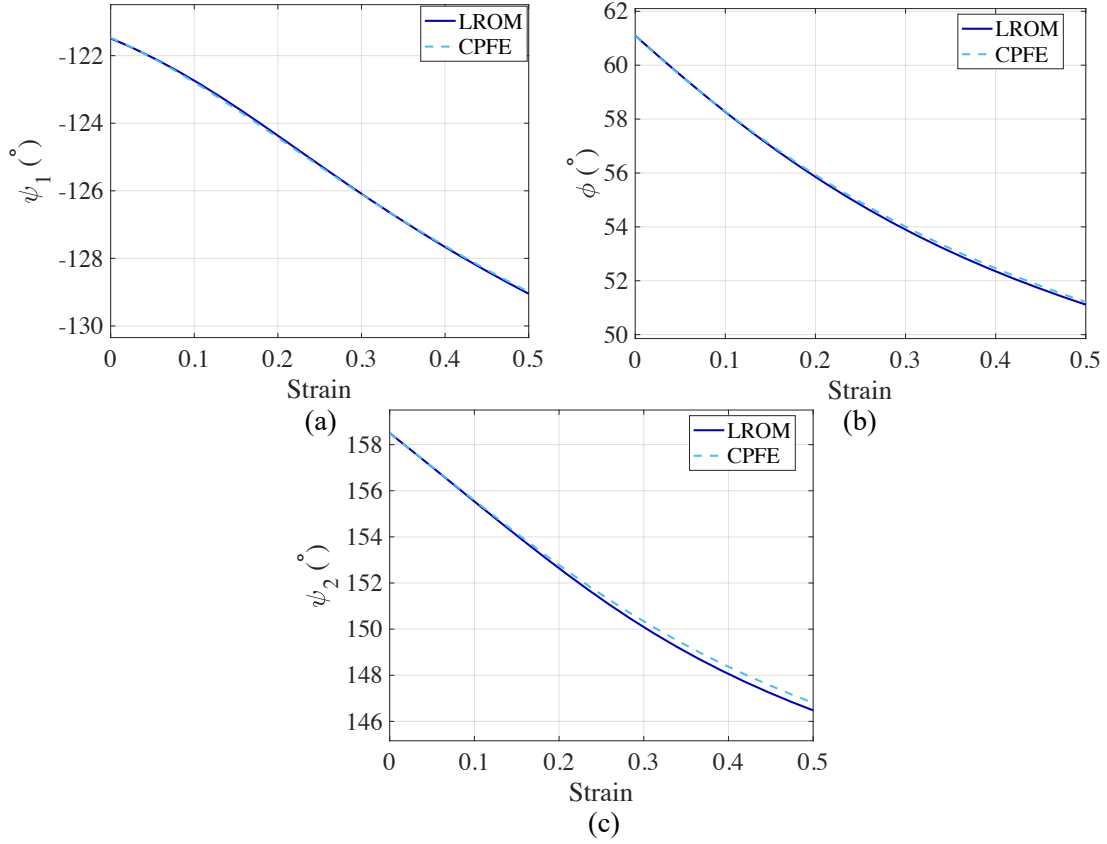


Figure 9: Euler angle evolution for voided RVE with diameter = $0.9 \mu\text{m}$, orientation 5 under simple shear loading: (a) (b) and (c) correspond to ψ_1 , ϕ and ψ_2 , respectively.

biaxial tension case, 50% strain is applied at constant strain rate of 0.5/s in the x direction and 30% strain is applied at constant strain rate of 0.3/s in the y direction.

Figure 7 shows the comparison of the overall stress-strain curves under the three loading conditions for a single crystal with $0.9 \mu\text{m}$ diameter void and crystal orientation 1 (Table 2). In addition to the reference CPFE simulation, the results of the LROM model are also compared with the Eigendeformation-based reduced order homogenization (EHM) model outlined in [27]. The EHM model relies on small strain assumption at the microscale and does not consider texture evolution. In the EHM simulations, large macroscopic strains are considered with corotational formulation. Under small deformations (e.g., when strain is less than 0.05), all three models yield similar stress-strain response. When the deformation becomes larger, EHM deviates from the reference CPFE simulation, while LROM continues to be reasonably accurate under all three loading configurations. The stress approximation error of the proposed LROM approach over all 25 cases (with 5 void fractions and 5 orientations) under the 3 loading conditions (i.e., a total of 75 simulations) are shown in Fig. 8. The stress approximation error is defined as follows

$$\text{error} = \int_0^\epsilon \frac{|\sigma_{\text{LROM}} - \sigma_{\text{CPFE}}|}{|\sigma_{\text{CPFE}}|} d\epsilon \quad (6.1)$$

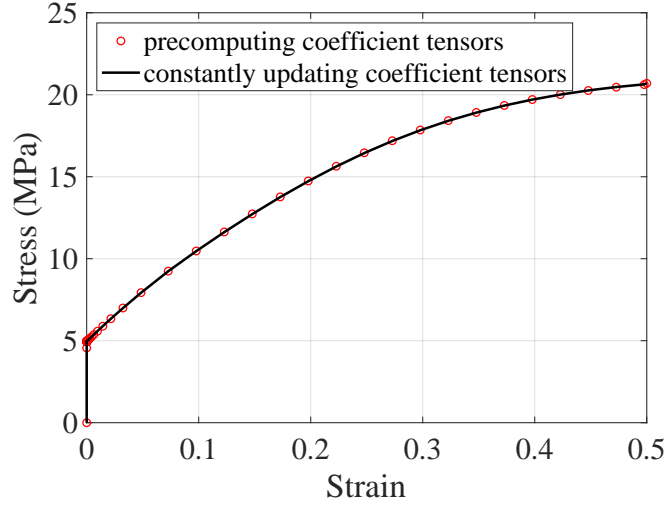


Figure 10: Comparison of precomputing and constantly updating the coefficient tensors.

The errors shown in Fig. 8 are averaged over the five orientations for each loading condition and geometry. The figure shows that the errors across different geometries, orientations and loading conditions remain under 2%.

Figure 9 shows the evolution of the three Euler angles as a function of macroscopic strain in the simple shear loading case as computed using the proposed and the reference CPFEE model. The reduced order model tracks a single crystal average orientation since model order is $n=1$. The void diameter is $0.9 \mu\text{m}$ and the initial crystal orientation is orientation 5. The values reported for CPFEE are also the volume averaged quantities over the microstructure. The plots indicate a significant deviation of the average crystal orientation of up to 11° at 50% strain level. The figures indicate a close match between the results of the LROM and CPFEE simulations. The orientation evolution within the crystal in CPFEE simulation shows stable distribution with maximum variation of 1° for the example shown above, indicating the volume averaged quantity is a good representation of the orientation in CPFEE model.

Figure 10 shows the results of two LROM simulations. These simulations consider void diameter of $0.9 \mu\text{m}$ and initial crystal orientation 1 with uniaxial tension loading condition. In the first case, coefficient tensors $\mathbf{A}^{(\alpha)}$, $\mathbf{M}^{(\beta\alpha)}$, $\mathbf{P}^{(\beta\alpha)}$, $\mathbf{S}^{(\alpha)}$ and $\mathbf{T}^{(\beta\alpha)}$ are updated at the end of every increment. The update entails recomputing the influence functions with updated texture and performing the corresponding integrations to obtain the coefficient tensors. In the second case, the coefficient tensors are pre-computed at the preprocessing stage and kept constant throughout the simulation. In the present case, Figure 10 demonstrates that evolution of the coefficient tensors does not affect the computed stress-strain response within 50% strain range.

6.2. Synthetic polycrystalline simulations

The capabilities of the proposed reduced order approach is further verified on polycrystalline configurations. Three polycrystalline microstructures as shown in Fig. 11 are employed. The microstructures consist of 57, 91 and 134 randomly oriented and equiaxed FCC grains. The grain

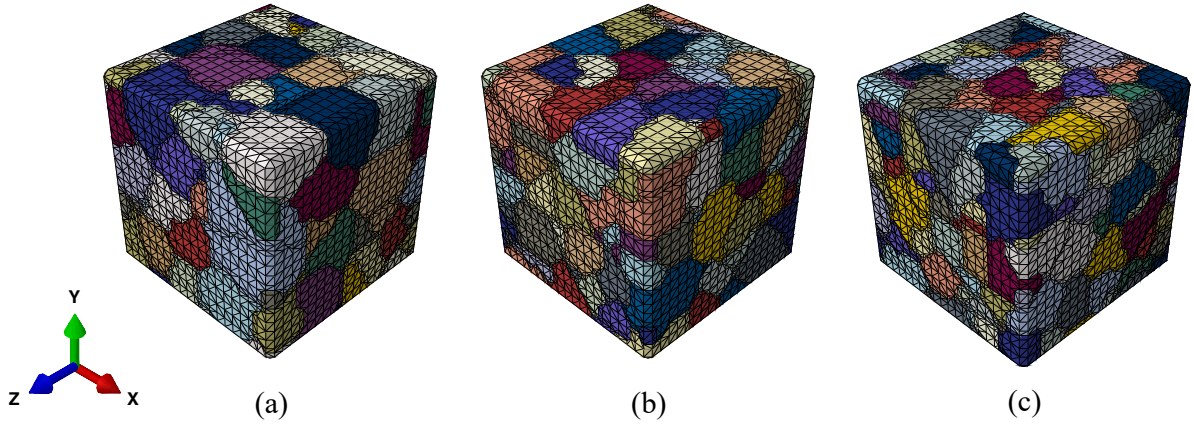


Figure 11: Three microstructures with different sizes: (a) 57-grain, (b) 91-grain and (c) 134-grain.

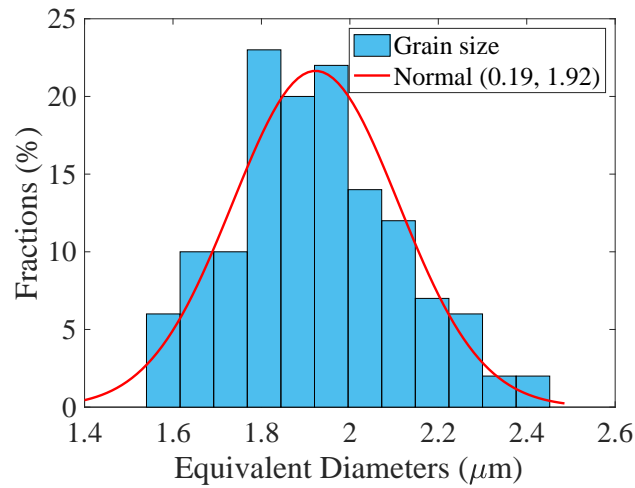


Figure 12: Grain size distribution of the 57-grain RVE with actual grain size.

sizes are sampled from a normal distribution shown in Fig. 12. The figure also shows the sampled distribution for the 57-grain microstructure. The orientation of the grains are randomly sampled from a uniformed distribution, and the microstructures do not exhibit significant elastic anisotropy. The microstructure are subjected to uniaxial, shear and biaxial loading conditions as described for the single crystal example.

The reference CPFEM simulations and influence function computations are performed using microstructure discretizations that contain 125,557, 138,600 and 157,926 elements for the three microstructures with respectively increasing number of grains. For the proposed approach, a single trilinear hexahedron is employed in the discretization of the macroscale domain, identical to the single crystal example. A part-per-grain scheme is adopted for the LROM representation of the microstructure.

The overall stress-strain curves computed by the proposed and reference models on the 57-grain microstructure under three load cases are shown in Fig. 13. Within the range of applied

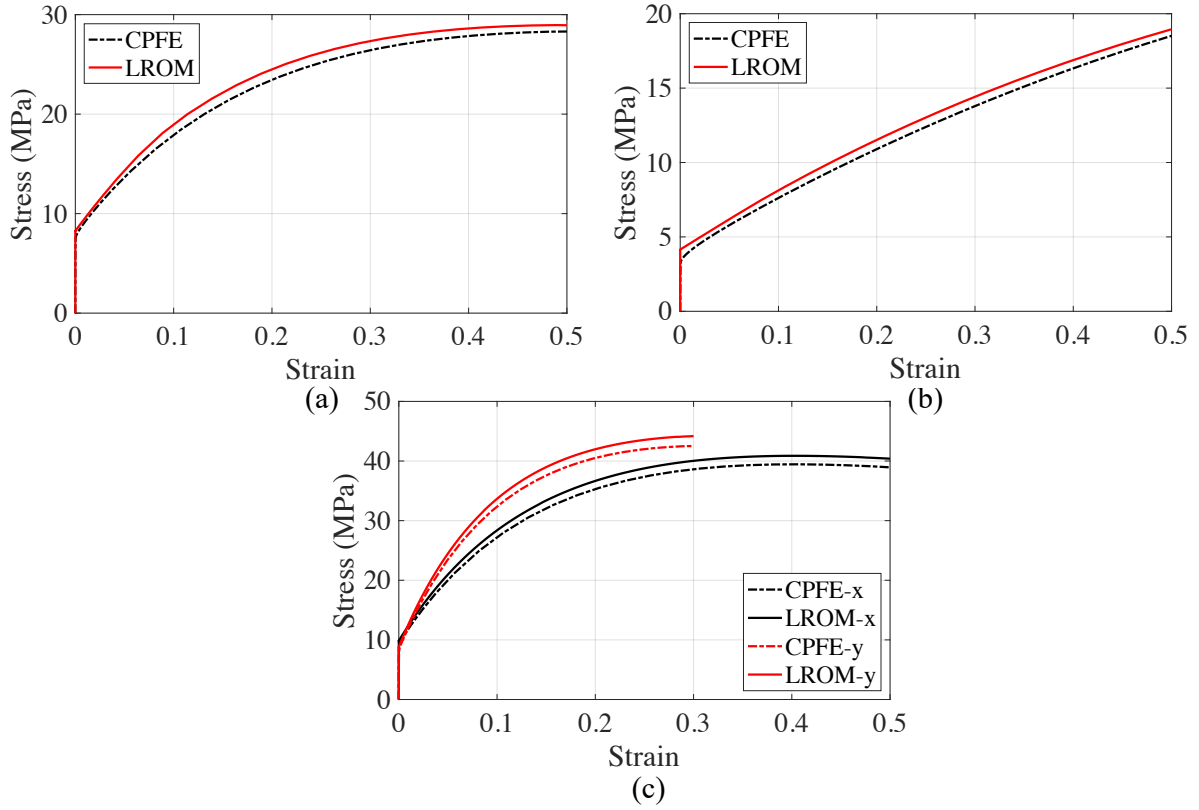


Figure 13: Overall stress-strain behavior of the 57-grain microstructure subjected to: (a) uniaxial tension; (b) simple shear; and (c) biaxial tension.

strains (50% engineering strain) the results exhibit a reasonable match between the CPFE and LROM simulations. The deformed configurations under the three loadings are shown in Fig. 14 to provide visual illustration of the extent of deformation that the microstructure undergo (from the CPFE simulations).

In order to ensure the consistency of model accuracy, 60 separate uniaxial tension simulations are performed for each of the three microstructural configurations for a total of 180 simulations. In each simulation, the grain orientations are resampled from the uniform distribution. Figure 15 displays the errors for the stress-strain behavior for all 180 cases as a histogram chart. The approximation error is computed using Eq. (6.1). For all cases, the LROM simulations exhibit errors less than 5%. As the microstructure size grows and hence gets closer to a size that is statistically representative with respect to the overall behavior, the variance and the mean error accordingly reduce.

To demonstrate the efficiency of the proposed model, the run time and speedup are also recorded for all 180 simulations of three RVEs. The averaged results for each of the three microstructures are shown in Table 3. The proposed LROM model exhibits a significant speedup compared with the CPFE simulations. For the 57-grain microstructure, the speedup is approximately 830, whereas for the 134-grain microstructure, the speedup drops to approximately 217.

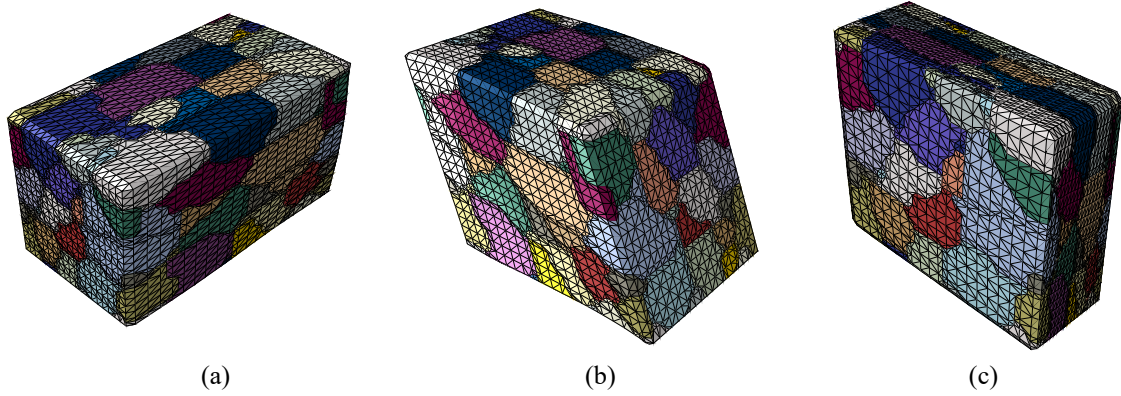


Figure 14: Deformed configurations of the 57-grain microstructure subjected to: (a) uniaxial tension; (b) simple shear; and (c) biaxial tension.

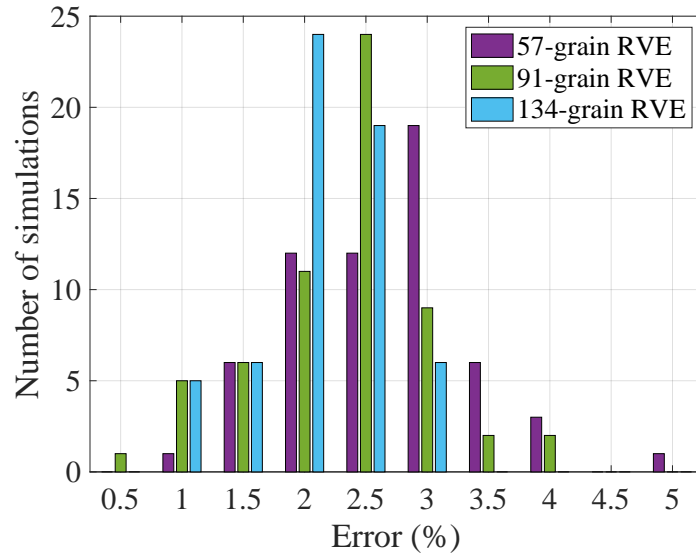


Figure 15: Overall stress approximation error distributions for synthetic RVEs.

Table 3: Average run time for three RVEs.

	LROM	CPFE	Speedup
57-grain	5.169 s	4289.041 s	829.762
91-grain	15.056 s	5062.775 s	336.263
134-grain	26.860 s	5825.240 s	216.874

The reduction of efficiency as a function of microstructure complexity is due to the fact that the reduced order system of equations result in dense Jacobian matrices. As reduced order system size gets larger, the efficiency gain compared to a sparse CPFE solver is reduced. In the context of small deformations, Zhang and Oskay [28] proposed a sparse reduced order model based on neglecting some long range interactions within the microstructure. A similar approach could re-

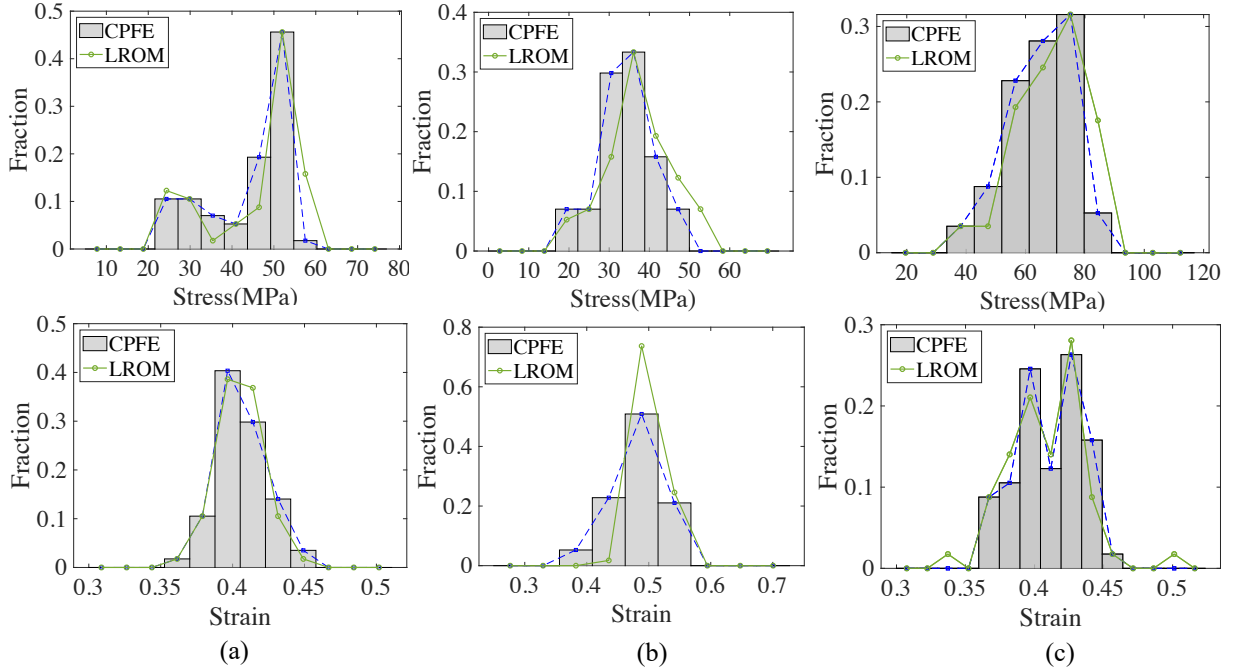


Figure 16: Local Mises stress (top row) and principal strain (bottom row) for the polycrystal microstructure subjected to: (a) uniaxial tension; (b) simple shear; and (c) biaxial tension loadings.

sult in higher efficiencies for larger microstructures, and will be investigated in the future for large deformation.

In addition to the overall stress responses, we also tested the ability of the proposed reduced order model to capture local stresses within the microstructures. Figure 16 shows the comparison of the grain-averaged Mises stress and principal strain distributions within the microstructures as computed by the proposed approach and the CPFE simulations for all three loading conditions applied to the 57-grain microstructure. The bin plots represent the CPFE model whereas the circles plotted at the mid-point of each bin refer to the results of the proposed model. The magnitudes of the local stresses match reasonably well with those of the CPFE simulations with slight overestimation. This slight overestimation is consistent with the stiffer overall stress-strain curves in Fig. 13 due to constrained kinematics associated with the reduced basis. The grain-average principal strains are also in reasonable agreement with each other, particularly for uniaxial and biaxial conditions. The results of the shear case indicated that the LROM predictions are concentrated slightly closer to the average compared with the CPFE model. Figure 17 shows the Mises stress contours within the microstructure as predicted by the LROM and CPFE simulations. The contour plots are from simple shear loading. The largest error of grain-average stresses across all is around 10%. Due to the “one-part-per-grain” partitioning scheme used in LROM, no intra-grain stress variation is captured with the model, whereas the CPFE simulation exhibits spatial variation within the grains.

Figure 18 compares the stress-strain curves for 5 randomly selected grains within the polycrystalline microstructure subjected to uniaxial tension loading. In addition to peak stress distribution

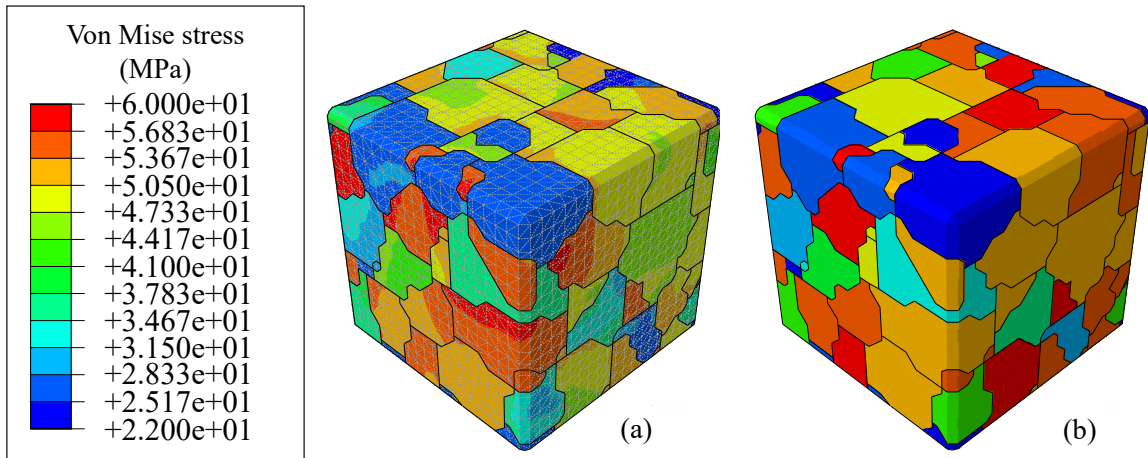


Figure 17: Local Mises stress contours for the 57-grain RVE: (a) CPFE simulation; (b) LROM simulation.

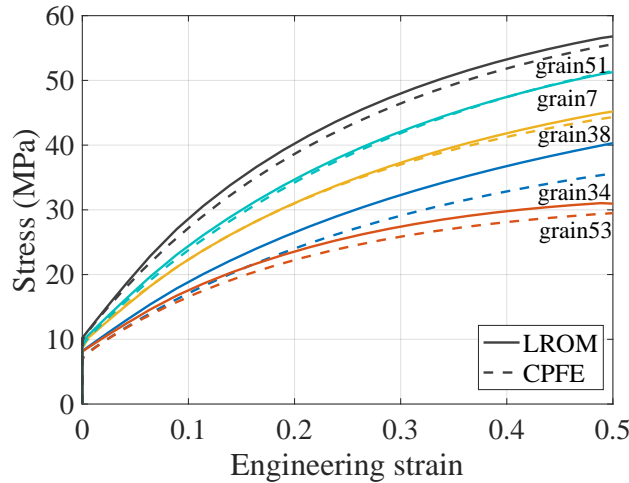


Figure 18: Stress-strain curve comparison of 5 randomly selected grains under uniaxial tension loading.

shown in Fig 7, the results indicate that the LROM captures the evolution of the local stresses in a reasonable fashion even when the microstructure deformation is extensive and individual grains undergo significant shape change (see Fig. 14(a)).

The texture evolution plays a very important role in the context of large deformation. Figure 19 shows the $\{111\}$ pole figures of the initial and final textures as computed using the LROM and CPFE simulations for the 134-grain microstructure under uniaxial tension. The initial texture shown in Fig. 19 (a) is generated from a uniform distribution and thus exhibits a scattered pattern. Figure 19 (b) and (c) both show oriented texture along the out of plane direction (i.e., along the direction of the applied load in the Z direction; $\{111\}$ pole figure represents XY plane). The LROM computation of the final texture matches reasonably well with that of the CPFE simulation.

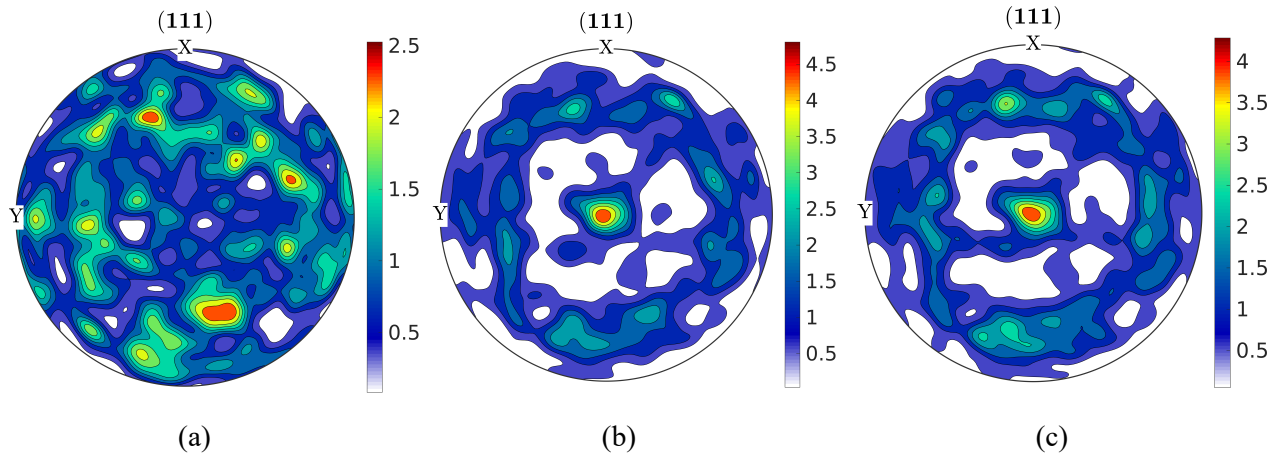


Figure 19: $\{111\}$ pole figure of the (a) initial texture; (b) final texture from LROM; and (c) final texture from CPFЕ.

7. Conclusion

This manuscript presented a novel reduced order multiscale approach for large deformation response of polycrystalline materials generalizing the ideas of EHM. The proposed approach is verified against crystal plasticity finite element simulations for single- and polycrystal characteristic volumes. Both overall and local mechanical responses, and texture evolution show reasonable accuracy compared with CPFЕ simulations, but at a fraction of the computational cost.

Two challenges still remain for the current framework. First, the proposed formulation is based on rigid-viscoplastic behavior. The generalization of the present formulation to accommodate elastic-viscoplastic constitutive behavior could provide more accurate response in large structural scenarios, where different parts of a structure undergo different levels of inelastic material deformation. Second, problems that impose time varying strain rates may result in significant changes in the coefficient tensors as a function of deformation. As mentioned in the manuscript, frequent coefficient tensor update could lead to prohibitive computational cost. Possible strategies such as selectively updating the coefficient tensors or employing surrogate modeling (e.g., machine learning) for the coefficient tensor computation may result in efficient and accurate reduced order models in such scenarios.

8. Acknowledgments

The authors gratefully acknowledge the support from the National Science Foundation provided through the IPA IR/D Program.

Bibliography

- [1] J. Guedes, N. Kikuchi, Preprocessing and postprocessing for materials based on the homogenization method with adaptive finite element methods, *Computer Methods in Applied Mechanics and Engineering* 83 (2) (1990) 143–198.

- [2] T. J. Hughes, G. R. Feijóo, L. Mazzei, J. B. Quincy, The variational multiscale method a paradigm for computational mechanics, *Computer Methods in Applied Mechanics and Engineering* 166 (1-2) (1998) 3–24.
- [3] C. Oskay, Variational multiscale enrichment for modeling coupled mechano-diffusion problems, *International Journal for Numerical Methods in Engineering* 89 (6) (2012) 686–705.
- [4] S. Zhang, C. Oskay, Variational multiscale enrichment method with mixed boundary conditions for elasto-viscoplastic problems, *Computational Mechanics* 55 (4) (2015) 771–787.
- [5] C. Oskay, Variational multiscale enrichment method with mixed boundary conditions for modeling diffusion and deformation problems, *Computer Methods in Applied Mechanics and Engineering* 264 (2013) 178–190.
- [6] T. Y. Hou, X. Wu, A multiscale finite element method for elliptic problems in composite materials and porous media, *Journal of Computational Physics* 134 (1) (1997) 169–189.
- [7] A. Abdulle, E. Weinan, B. Engquist, E. Vanden-Eijnden, The heterogeneous multiscale method, *Acta Numerica* 21 (2012) 1–87.
- [8] D. Peirce, R. Asaro, A. Needleman, An analysis of nonuniform and localized deformation in ductile single crystals, *Acta Metallurgica* 30 (6) (1982) 1087–1119.
- [9] R. J. Asaro, Micromechanics of crystals and polycrystals, *Advances in Applied Mechanics* 23 (1) (1983) 115.
- [10] D. Peirce, R. J. Asaro, A. Needleman, Material rate dependence and localized deformation in crystalline solids, *Acta Metallurgica* 31 (12) (1983) 1951–1976.
- [11] E. B. Marin, On the formulation of a crystal plasticity model., Tech. rep., Sandia National Laboratories (2006).
- [12] J. T. Benzinger, Y. Liu, X. Zhang, W. E. Luecke, D. Ponge, A. Dutta, C. Oskay, D. Raabe, J. E. Wittig, Experimental and numerical study of mechanical properties of multi-phase medium-mn twip-trip steel: Influences of strain rate and phase constituents, *Acta Materialia* 177 (2019) 250–265.
- [13] X. Zhang, C. Oskay, Plastic dissipation sensitivity to mechanical properties in polycrystalline β -hmx subjected to impact loading, *Mechanics of Materials* 138 (2019) 103079.
- [14] Y. Liu, Y. Zhu, C. Oskay, P. Hu, L. Ying, D. Wang, Experimental and computational study of microstructural effect on ductile fracture of hot-forming materials, *Materials Science and Engineering: A* 724 (2018) 298–323.
- [15] G. Sachs, Zur ableitung einer fließbedingung, in: *Mitteilungen der Deutschen Materialprüfungsanstalten*, Springer, 1929, pp. 94–97.
- [16] G. I. Taylor, Plastic strain in metals, *Journal of the Institute of Metals* 62 (1938) 307–324.
- [17] P. Turner, C. Tomé, C. Woo, Self-consistent modelling of nonlinear visco-elastic polycrystals: an approximate scheme, *Philosophical Magazine A* 70 (4) (1994) 689–711.
- [18] J. Hutchinson, Elastic-plastic behaviour of polycrystalline metals and composites, *Proceedings of the Royal Society of London. A. Mathematical and Physical Sciences* 319 (1537) (1970) 247–272.
- [19] H. Moulinec, P. Suquet, A numerical method for computing the overall response of nonlinear composites with complex microstructure, *Computer Methods in Applied Mechanics and Engineering* 157 (1-2) (1998) 69–94.
- [20] R. A. Lebensohn, A. K. Kanjarla, P. Eisenlohr, An elasto-viscoplastic formulation based on fast fourier transforms for the prediction of micromechanical fields in polycrystalline materials, *International Journal of Plasticity* 32 (2012) 59–69.
- [21] J. C. Michel, P. Suquet, Computational analysis of nonlinear composite structures using the nonuniform transformation field analysis, *Computer Methods in Applied Mechanics and Engineering* 193 (48-51) (2004) 5477–5502.
- [22] J. C. Michel, P. Suquet, A model-reduction approach in micromechanics of materials preserving the variational structure of constitutive relations, *Journal of the Mechanics and Physics of Solids* 90 (2016) 254–285.
- [23] J. Hernández, J. Oliver, A. E. Huespe, M. Caicedo, J. Cante, High-performance model reduction techniques in computational multiscale homogenization, *Computer Methods in Applied Mechanics and Engineering* 276 (2014) 149–189.
- [24] Z. Liu, M. Bessa, W. K. Liu, Self-consistent clustering analysis: an efficient multi-scale scheme for inelastic heterogeneous materials, *Computer Methods in Applied Mechanics and Engineering* 306 (2016) 319–341.
- [25] Z. Liu, O. L. Kafka, C. Yu, W. K. Liu, Data-driven self-consistent clustering analysis of heterogeneous materials with crystal plasticity, in: *Advances in Computational Plasticity*, Springer, 2018, pp. 221–242.
- [26] Z. Liu, M. Fleming, W. K. Liu, Microstructural material database for self-consistent clustering analysis of elasto-plastic strain softening materials, *Computer Methods in Applied Mechanics and Engineering* 330 (2018) 547–

577.

- [27] X. Zhang, C. Oskay, Eigenstrain based reduced order homogenization for polycrystalline materials, *Computer Methods in Applied Mechanics and Engineering* 297 (2015) 408–436.
- [28] X. Zhang, C. Oskay, Sparse and scalable eigenstrain-based reduced order homogenization models for polycrystal plasticity, *Computer Methods in Applied Mechanics and Engineering* 326 (2017) 241–269.
- [29] Y. Liu, X. Zhang, Y. Zhu, P. Hu, C. Oskay, Dislocation density informed eigenstrain based reduced order homogenization modeling: verification and application on a titanium alloy structure subjected to cyclic loading, *Modelling and Simulation in Materials Science and Engineering* 28 (2) (2020) 025004.
- [30] X. Zhang, Y. Liu, C. Oskay, Multiscale reduced-order modeling of a titanium skin panel subjected to thermo-mechanical loading, *arXiv preprint arXiv:2011.03907* (2020).
- [31] Z. Liu, C. Wu, M. Koishi, A deep material network for multiscale topology learning and accelerated nonlinear modeling of heterogeneous materials, *Computer Methods in Applied Mechanics and Engineering* 345 (2019) 1138–1168.
- [32] Z. Liu, C. Wu, M. Koishi, Transfer learning of deep material network for seamless structure–property predictions, *Computational Mechanics* 64 (2) (2019) 451–465.
- [33] Z. Liu, Deep material network with cohesive layers: Multi-stage training and interfacial failure analysis, *Computer Methods in Applied Mechanics and Engineering* 363 (2020) 112913.
- [34] R. A. Lebensohn, C. Tomé, A self-consistent anisotropic approach for the simulation of plastic deformation and texture development of polycrystals: application to zirconium alloys, *Acta Metallurgica et Materialia* 41 (9) (1993) 2611–2624.
- [35] A. Molinari, G. Canova, S. Ahzi, A self consistent approach of the large deformation polycrystal viscoplasticity, *Acta Metallurgica* 35 (12) (1987) 2983–2994.
- [36] A. Molinari, S. Ahzi, R. Kouddane, On the self-consistent modeling of elastic-plastic behavior of polycrystals, *Mechanics of Materials* 26 (1) (1997) 43–62.
- [37] H. Wang, P. Wu, C. Tomé, Y. Huang, A finite strain elastic–viscoplastic self-consistent model for polycrystalline materials, *Journal of the Mechanics and Physics of Solids* 58 (4) (2010) 594–612.
- [38] J. Segurado, R. A. Lebensohn, J. LLorca, C. N. Tomé, Multiscale modeling of plasticity based on embedding the viscoplastic self-consistent formulation in implicit finite elements, *International Journal of Plasticity* 28 (1) (2012) 124–140.
- [39] P. Eisenlohr, M. Diehl, R. A. Lebensohn, F. Roters, A spectral method solution to crystal elasto-viscoplasticity at finite strains, *International Journal of Plasticity* 46 (2013) 37–53.
- [40] N. Lahellec, J. C. Michel, H. Moulinec, P. Suquet, Analysis of inhomogeneous materials at large strains using fast fourier transforms, in: *IUTAM symposium on computational mechanics of solid materials at large strains*, Springer, 2003, pp. 247–258.
- [41] J. Michel, H. Moulinec, P. Suquet, A computational scheme for linear and non-linear composites with arbitrary phase contrast, *International Journal for Numerical Methods in Engineering* 52 (1-2) (2001) 139–160.
- [42] J. S. Nagra, A. Brahme, R. A. Lebensohn, K. Inal, Efficient fast fourier transform-based numerical implementation to simulate large strain behavior of polycrystalline materials, *International Journal of Plasticity* 98 (2017) 65–82.
- [43] T. De Geus, J. Vondřejc, J. Zeman, R. Peerlings, M. Geers, Finite strain fft-based non-linear solvers made simple, *Computer Methods in Applied Mechanics and Engineering* 318 (2017) 412–430.
- [44] M. Kabel, S. Fliegerer, M. Schneider, Mixed boundary conditions for fft-based homogenization at finite strains, *Computational Mechanics* 57 (2) (2016) 193–210.
- [45] A. Eghtesad, M. Zecevic, R. A. Lebensohn, R. J. McCabe, M. Knezevic, Spectral database constitutive representation within a spectral micromechanical solver for computationally efficient polycrystal plasticity modelling, *Computational Mechanics* 61 (1-2) (2018) 89–104.
- [46] M. Zecevic, R. J. McCabe, M. Knezevic, A new implementation of the spectral crystal plasticity framework in implicit finite elements, *Mechanics of Materials* 84 (2015) 114–126.
- [47] P. Shanthraj, P. Eisenlohr, M. Diehl, F. Roters, Numerically robust spectral methods for crystal plasticity simulations of heterogeneous materials, *International Journal of Plasticity* 66 (2015) 31–45.
- [48] P. Van Houtte, S. Li, M. Seefeldt, L. Delannay, Deformation texture prediction: from the taylor model to the

- advanced lamel model, *International Journal of Plasticity* 21 (3) (2005) 589–624.
- [49] D. Tjahjanto, P. Eisenlohr, F. Roters, A novel grain cluster-based homogenization scheme, *Modelling and Simulation in Materials Science and Engineering* 18 (1) (2009) 015006.
- [50] C. Yu, O. L. Kafka, W. K. Liu, Self-consistent clustering analysis for multiscale modeling at finite strains, *Computer Methods in Applied Mechanics and Engineering* 349 (2019) 339–359.
- [51] M. Shakoor, O. L. Kafka, C. Yu, W. K. Liu, Data science for finite strain mechanical science of ductile materials, *Computational Mechanics* 64 (1) (2019) 33–45.
- [52] M. Yuan, S. Paradiso, B. Meredig, S. R. Niezgod, Machine learning-based reduce order crystal plasticity modeling for icme applications, *Integrating Materials and Manufacturing Innovation* 7 (4) (2018) 214–230.
- [53] S. Kok, A. J. Beaudoin, D. A. Tortorelli, A polycrystal plasticity model based on the mechanical threshold, *International Journal of Plasticity* 18 (5-6) (2002) 715–741.
- [54] J. R. Rice, Inelastic constitutive relations for solids: an internal-variable theory and its application to metal plasticity, *Journal of the Mechanics and Physics of Solids* 19 (6) (1971) 433–455.
- [55] M. Kothari, L. Anand, Elasto-viscoplastic constitutive equations for polycrystalline metals: application to tantalum, *Journal of the Mechanics and Physics of Solids* 46 (1) (1998) 51–83.
- [56] V. Kouznetsova, M. G. Geers, W. M. Brekelmans, Multi-scale constitutive modelling of heterogeneous materials with a gradient-enhanced computational homogenization scheme, *International journal for numerical methods in engineering* 54 (8) (2002) 1235–1260.
- [57] J. Fish, R. Fan, Mathematical homogenization of nonperiodic heterogeneous media subjected to large deformation transient loading, *International Journal for Numerical Methods in Engineering* 76 (7) (2008) 1044–1064.
- [58] J. Fish, S. Kuznetsov, Computational continua, *International Journal for Numerical Methods in Engineering* 84 (7) (2010) 774–802.
- [59] A. Bensoussan, J. L. Lions, G. Papanicolaou, *Asymptotic analysis for periodic structures*, Vol. 374, American Mathematical Soc., 2011.
- [60] C. Oskay, J. Fish, Eigendeformation-based reduced order homogenization for failure analysis of heterogeneous materials, *Computer Methods in Applied Mechanics and Engineering* 196 (7) (2007) 1216–1243.
- [61] J. C. Simo, T. J. Hughes, *Computational inelasticity*, Vol. 7, Springer Science & Business Media, 2006.